

# Hold me tight! Influence of discriminative features on deep network boundaries

Guillermo Ortiz-Jiménez\*  
EPFL

guillermo.ortizjimenez@epfl.ch

Apostolos Modas\*  
EPFL

apostolos.modas@epfl.ch

Seyed-Mohsen Moosavi-Dezfooli  
ETH Zürich  
seyed.moosavi@inf.ethz.ch

Pascal Frossard  
EPFL  
pascal.frossard@epfl.ch

## Abstract

Important insights towards the explainability of neural networks reside in the characteristics of their decision boundaries. In this work, we borrow tools from the field of adversarial robustness, and propose a new perspective that relates dataset features to the distance of samples to the decision boundary. This enables us to carefully tweak the position of the training samples and measure the induced changes on the boundaries of CNNs trained on large-scale vision datasets. We use this framework to reveal some intriguing properties of CNNs. Specifically, we rigorously confirm that neural networks exhibit a high invariance to non-discriminative features, and show that very small perturbations of the training samples in certain directions can lead to sudden invariances in the orthogonal ones. This is precisely the mechanism that adversarial training uses to achieve robustness.

## 1 Introduction

The set of points that partitions the input space onto labeled regions is known as the *decision boundary* of a classifier. Describing how a classifier creates such boundaries is crucial for its explainability. Interestingly, even when deep networks succeed on a task, their high vulnerability to imperceptible perturbations [1, 2] implies that their boundaries lie alarmingly close to any input sample. This unintuitive behaviour contradicts the common belief that a successful classifier should be invariant to non-discriminative information of its input data. However, it seems that such perturbations are not irrelevant signals, but rather discriminative features of the training set [3, 4].

In that sense, explaining the mechanisms that construct the decision boundary of deep neural networks is key to understand the dynamics of adversarial training [5]. This training scheme only differs from standard training in that it slightly perturbs the training samples during optimization. However, these small changes can utterly change the geometry of these classifiers [6].

An example of such change can be seen in Fig. 1, which shows the minimal perturbations – constrained to lie on a low and a high frequency subspace – required to flip the decision of a

---

\*Equal contribution. Correspondence to {guillermo.ortizjimenez, apostolos.modas}@epfl.ch

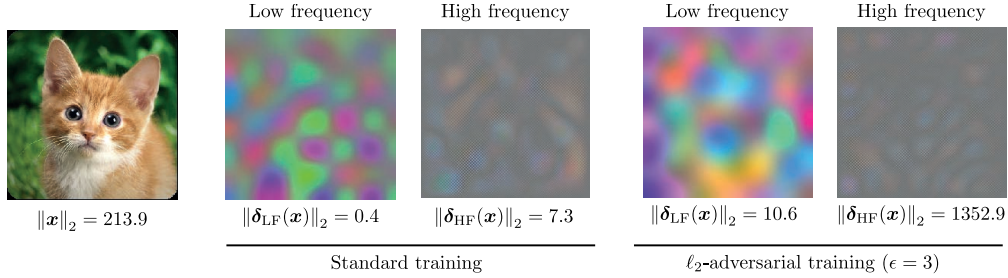


Figure 1: Minimal adversarial perturbations constrained to lie in different DCT frequency bands ( $8 \times 8$  subspaces taken from the top left and bottom right of the  $224 \times 224$  DCT matrix) for a ResNet-50 trained (**top**), and adversarially trained (**bottom**) on ImageNet.

network. The norm of the perturbations measures the distance (margin) to the decision boundary in these subspaces. Clearly, reaching the boundary using high frequency perturbations requires much more energy than using low frequency ones [7]. But surprisingly, when the network is adversarially trained [5], the largest increase in margin happens in the high frequency subspace. Note that, on the standard network, this distance is already much greater than the size of the training perturbations. Based on this observation, we pose the following questions:

1. *How is the margin in different directions related to the features in the training data?*
2. *How can very small perturbations significantly change the geometry of deep networks?*

In this work, we propose a novel approach to answer these questions. In particular, we develop a new methodology to construct a local summary of the decision boundary of a neural network from margin observations along a sequence of orthogonal directions. This framework permits to carefully tweak the properties of the training samples and measure the induced changes on the boundaries of convolutional neural networks (CNNs) trained on synthetic and large-scale vision datasets (e.g., ImageNet). The main contributions of our work are the following:

1. We provide a new perspective on the relationship between the distance of a set of samples to the boundary, and the discriminative features used by a network. We empirically support our findings by extensive evaluations on both synthetic and real datasets.
2. Via a series of carefully designed experiments, we rigorously confirm the “common belief” that CNNs tend to behave as ideal classifiers and are approximately invariant to non-discriminative features of a dataset.
3. We further show that the construction of the decision boundary is extremely sensitive to the position of the training samples, such that very small perturbations in certain directions can utterly change the decision boundaries in some orthogonal directions.
4. Finally, we demonstrate that adversarial training exploits this training sensitivity and invariance bias to build robust classifiers.

We believe that the perspective proposed in this paper can have implications in future research on explainability and robustness, as it gives a new way to measure and understand decision boundaries. This new framework can be used to shed light onto the dynamics and inductive bias of deep learning.

**Related work** Since the publication of [8], a big body of research has focused on understanding the inductive bias of deep networks as a way to explain generalization in deep learning [9, 10]. Remarkably, for linear classifiers, optimizing a logistic loss using gradient descent is equivalent to maximizing margin in the input space [11]. Furthermore, for deep networks, some recent results suggest that margin is maximized in the logit space [12].

Interestingly, recent works have established the link between adversarial perturbations and discriminative features of the training sets [3, 4, 13]. This has led to the conjecture that, in most datasets, there exist robust and non-robust features that neural networks exploit to construct their decision boundaries. What exactly are these features, and how do networks construct these boundaries is however not addressed by these authors. In this sense, the authors of [14] argue that the excessive invariance in the boundaries introduced by adversarial training can explain its induced decrease in accuracy. In this work, we shed light on these phenomena, by describing the strong inductive bias of the networks towards invariance to non-discriminative features, and the sensitivity of training to small perturbations.

The geometric properties of the decision boundaries of deep networks have previously been studied, mainly focused on their curvature [6, 15], and their decision region topology [15, 16]. From a robustness perspective, the distance to the boundary has been exploited to detect adversarial examples [17] and predict generalization gap [18, 19]. Furthermore, the unusual robustness of deep networks in certain frequencies [7, 20, 21] has recently been described. In this work, however, we give a constructive explanation for this phenomenon based on the role of dataset features in shaping the margins along different frequencies.

## 2 Proposed framework

Let  $f : \mathbb{R}^D \rightarrow \mathbb{R}^L$  be the final layer of a neural network (i.e., logits), such that, for any input  $\mathbf{x} \in \mathbb{R}^D$ ,  $F(\mathbf{x}) = \operatorname{argmax}_k f_k(\mathbf{x})$  represents the decision function of that network, where  $f_k(\mathbf{x})$  denotes the  $k$ th component of  $f(\mathbf{x})$  that corresponds to the  $k$ th class. The decision boundary between classes  $k$  and  $\ell$  of a neural network is the set  $\mathcal{B}_{k,\ell}(f) = \{\mathbf{x} \in \mathbb{R}^D : f_k(\mathbf{x}) - f_\ell(\mathbf{x}) = 0\}$  (in general, we will omit the dependency with  $k, \ell$  for simplicity). Unless stated otherwise, we assume that all networks are trained using a cross-entropy loss function and some variant of (stochastic) gradient descent. We also assume that training has been conducted for many epochs, and that it has approximately converged to a local minimum of the loss, achieving 100% accuracy on the training data [8]<sup>1</sup>.

In this work, we study the role that the training set  $\mathcal{T} = \{(\mathbf{x}^{(i)}, y^{(i)})\}_{i=0}^{N-1}$  has on the boundary  $\mathcal{B}(f)$ . Specifically, we propose to use adversarial proxies to measure the distribution of distances to the decision boundary along a sequence of well defined subspaces. The main quantities of interest are:

**Definition 1** (Minimal adversarial perturbations). *Given a classifier  $F$ , a sample  $\mathbf{x} \in \mathbb{R}^D$ , and a sub-region of the input space  $\mathcal{S} \subseteq \mathbb{R}^D$ , we define the ( $\ell_2$ ) minimal adversarial perturbation of  $\mathbf{x}$  in  $\mathcal{S}$  as*

$$\delta_{\mathcal{S}}(\mathbf{x}) = \operatorname{argmin}_{\delta \in \mathcal{S}} \|\delta\|_2 \quad \text{s.t.} \quad F(\mathbf{x} + \delta) \neq F(\mathbf{x}).$$

*In general, whenever  $\mathbf{u} \in \mathbb{S}^{D-1}$  denotes a unit-norm vector in  $\mathbb{R}^D$  (direction) we will use  $\delta_{\mathbf{u}}(\mathbf{x})$  meaning  $\delta_{\operatorname{span}\{\mathbf{u}\}}(\mathbf{x})$ . Similarly, we will use  $\delta(\mathbf{x})$  to refer to  $\delta_{\mathbb{R}^D}(\mathbf{x})$ .*

---

<sup>1</sup>In general all details of our experiments are listed in the Supp. material.

**Definition 2** (Margin). *The magnitude  $\|\delta_S(\mathbf{x})\|_2$  is the margin of  $\mathbf{x}$  in  $\mathcal{S}$ .*

Our main objective is to obtain a local summary of  $\mathcal{B}(f)$  around a set of observation samples  $\mathcal{O} = \{\mathbf{x}^{(i)}\}_{i=0}^{M-1}$  by measuring their margin in a sequence of distinct subspaces  $\{\mathcal{S}_j\}_{j=0}^{R-1}$ . In practice, we use a subspace-constrained version of DeepFool [22]<sup>2</sup> to approximate the margins in each  $\mathcal{S}_j$ .

### 3 Margin and discriminative features

As known from previous studies on the robustness of deep learning [23], the distance from a sample to the boundary of a neural network can vary greatly depending on the search direction. This behaviour is generally translated into classifiers with small margins along some directions, and large margins along the others. In this section, we show that the small margin directions are associated with discriminative directions, and we provide a constructive procedure to identify them. This helps us to shed new light into the inductive bias of the training dynamics of neural networks.

#### 3.1 Evidence on synthetic data

We want to show that neural networks only construct boundaries along discriminative features, and that they are invariant in every other direction<sup>3</sup>. To this end, we generate a balanced training set  $\mathcal{T}_1(\epsilon, \sigma)$  by independently sampling  $N$  points  $\mathbf{x}^{(i)} = \mathbf{U}(\mathbf{x}_1^{(i)} \oplus \mathbf{x}_2^{(i)})$  such that  $\mathbf{x}_1^{(i)} = \epsilon \mathbf{y}^{(i)}$  and  $\mathbf{x}_2^{(i)} \sim \mathcal{N}(0, \sigma^2 \mathbf{I}_{D-1})$ , where  $\oplus$  denotes the concatenation operator and  $\epsilon > 0$  the feature size, and  $D = 100$ . The labels  $y^{(i)}$  are uniformly sampled from  $\{-1, +1\}$ . The multiplication by a random orthonormal matrix  $\mathbf{U} \in \text{SO}(D)$  is performed to avoid any possible bias of the classifier towards the canonical basis. Note that this is a linearly separable dataset with a single discriminative feature parallel to  $\mathbf{u}_1$  (i.e., first row of  $\mathbf{U}$ ), and all other dimensions filled with non-discriminative noise.

To evaluate our hypothesis we train a heavily overparameterized multilayer perceptron (MLP) with 10 hidden layers of 500 neurons using SGD (test: 100.0%). Table 1 shows the margin statistics on the linearly separable direction  $\mathbf{u}_1$ ; its orthogonal complement  $\text{span}\{\mathbf{u}_1\}^\perp$ ; a fixed random subspace of dimension  $S$ ,  $\mathcal{S}_{\text{rand}} \subset \mathbb{R}^D$ ; and a fixed random subspace of the same dimensionality, but orthogonal to  $\mathbf{u}_1$ ,  $\mathcal{S}_{\text{orth}} \subset \text{span}\{\mathbf{u}_1\}^\perp$ . From these values we can see that along the direction where the discriminative feature lies, the margin is much smaller than in any other direction. Therefore, we can see that the classification function of this network is only creating a boundary in  $\mathbf{u}_1$  with median margin  $\epsilon/2$ , and that it is approximately invariant in  $\text{span}\{\mathbf{u}_1\}^\perp$ .

Comparing the margin values for  $\mathcal{S}_{\text{orth}}$  and  $\mathcal{S}_{\text{rand}}$  we see that, if the observation basis is not aligned with the features exploited by the network, the margin measurements might not be able to separate the small and large margin directions. Indeed, since  $\mathcal{S}_{\text{orth}}$  is orthogonal to the only discriminative direction  $\mathbf{u}_1$  we see that the margin values reported in this region are much higher than those reported in  $\mathcal{S}_{\text{rand}}$ . The reason for this is that the margin required to flip the label of a classifier in a randomly selected subspace is of the order of  $\sqrt{S/D}$  with high probability [23], and hence the non-trivial correlation of a random subspace with the discriminative features will always hide the differences between small and large margin directions.

<sup>2</sup>We do not enforce the  $[0, 1]^D$  box constraints on the adversarial images, as we are not interested in finding “plausible” adversarial perturbations, but in measuring the distance to  $\mathcal{B}(f)$ .

<sup>3</sup>This is indeed a desired property for any classification method, but note that for neural networks the existence of adversarial examples contests the idea of it being a reasonable assumption.

Table 1: Margin statistics of an MLP trained on  $\mathcal{T}_1(\epsilon = 5, \sigma = 1)$  along different directions ( $N = 10,000$ ,  $M = 1,000$ ,  $S = 3$ ).

	$\mathbf{u}_1$	$\text{span}\{\mathbf{u}_1\}^\perp$	$\mathcal{S}_{\text{ORTH}}$	$\mathcal{S}_{\text{RAND}}$
5-PERC.	1.74	4.85	30.68	17.21
MEDIAN	2.50	12.36	102.0	27.90
95-PERC.	3.22	31.60	229.5	80.61

Finally, the fluctuations in the values and the fact that the classifier is not completely invariant on  $\text{span}\{\mathbf{u}_1\}^\perp$  might indicate that the network has built a complex boundary. However, similar fluctuations and finite values in  $\text{span}\{\mathbf{u}_1\}^\perp$  would also be expected, even if the model was linear by construction and was perfectly separating the training data<sup>4</sup>.

### 3.2 Evidence on real data

In contrast to the synthetic data, where the discriminative features are known by construction, the exact description of the features presented in *real* datasets is usually not known. In order to identify these features and understand their connection to the local construction of the decision boundaries, we apply the proposed framework on standard computer vision datasets, and investigate if deep networks trained on real data also present high invariance along the non-discriminative directions of the dataset.

In our study, we train multiple networks on MNIST [24] and CIFAR-10 [25], and on ImageNet [26] we use several of the pretrained networks provided by PyTorch [27]<sup>5</sup>. Let  $W, H, C$  denote the width, height, and number of channels of the images in those datasets, respectively. In our experiments we use the 2-dimensional discrete cosine transform (2D-DCT) [28] basis of size  $H \times W$  to generate the observation subspaces. In particular, let  $\mathcal{D} \in \mathbb{R}^{H \times W \times H \times W}$  denote the 2D-DCT generating tensor, such that  $\text{vec}(\mathcal{D}(i, j, :, :) \otimes \mathbf{I}_C)$  represents one basis element of the image space. We generate the subspaces by sampling  $K \times K$  blocks from the diagonal of the DCT tensor using a sliding window with step-size  $T$ :

$$\mathcal{S}_j = \text{span}\{\text{vec}(\mathcal{D}(j \cdot T + k, j \cdot T + k, :, :) \otimes \mathbf{I}_C) \mid k = 0, \dots, K - 1\}.$$

The sliding window on the diagonal of the DCT gives a good trade-off between visualization abilities in simple one-dimensional plots, and a diverse sampling of the spatial spectrum of natural images, with a well-defined gradient flowing from low to high frequencies<sup>6</sup>. We observe in practice that the DCT basis is also quite aligned to the features of these datasets, and hence it can give precise information about the discriminative features exploited by the networks.

The margin distribution of the evaluated test samples is presented in the top of Fig. 2. For MNIST and ImageNet, the networks present a strong invariance along high frequency directions and small margin along low frequency ones. We will later show that this is related to the fact that these networks mainly exploit discriminative features in the low frequencies of these datasets. Notice,

<sup>4</sup>In Sec. A of Supp. material we provide a theoretical characterization of this effect for a linear classifier.

<sup>5</sup>Experiments on more CNNs (with similar findings) are presented in Sec. I of Supp. material.

<sup>6</sup>See Sec. I of Supp. material for a similar analysis including off-diagonal subspaces.

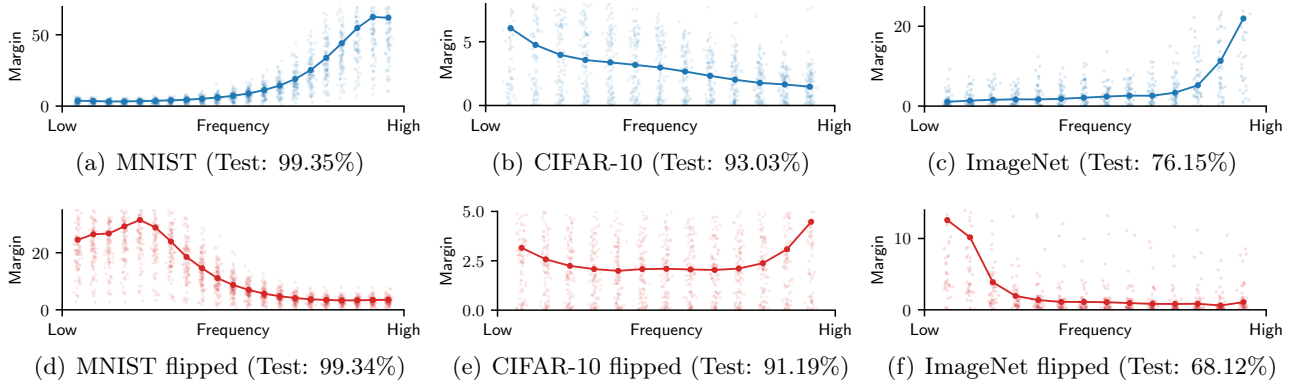


Figure 2: Margin distribution of test samples in subspaces taken from the diagonal of the DCT (low to high frequencies). The thick line indicates the median values of the margin, and the shaded points represent its distribution. **Top:** (a) MNIST (LeNet) [24], (b) CIFAR-10 (DenseNet-121) [29] and (c) ImageNet (ResNet-50) [30] **Bottom:** (d) MNIST (LeNet), (e) CIFAR-10 (DenseNet-121) and (f) ImageNet (ResNet-50) trained on frequency “flipped” versions of the standard datasets.

however, that for CIFAR-10 dataset the margin values are more uniformly distributed; an indication that the network exploits discriminative features across the full spectrum as opposed to the human vision system [31].

### 3.2.1 Adaptation to data representation

Towards verifying that the proposed framework can capture the relation between the data features and the local construction of the decision boundaries, we must first ensure that the direction of the observed invariance (large margin) is related to the features presented in the dataset, rather than being just an effect of the network itself.

Based on our observation that the margin tends to be small in low frequency directions and large in high frequency ones, we choose to carefully tweak the representation of the data, such that the low frequencies are swapped with the high frequencies. In practice, if  $\mathfrak{D}$  denotes the forward DCT transform operator, the new image representation  $\mathbf{x}'$  is expressed as  $\mathbf{x}' = \mathfrak{D}^{-1}(\text{flip}(\mathfrak{D}(\mathbf{x})))$ , where flip corresponds to one horizontal and one vertical flip of the DCT transformed image<sup>7</sup>. Thus, if the direction of the resulting margin is strongly related to the data features, the constructed decision boundaries should also adapt to this new data representation, and the margin along the invariant directions (high frequencies) should swap with the margin of the discriminative ones (low frequencies). Informally speaking, the margin distribution should “flip”.

We apply our framework on multiple networks trained on the “flipped” datasets, and the margin distribution is depicted at the bottom of Fig. 2. For both MNIST and ImageNet, the directions of the decision boundaries indeed *follow* the new data representation – although they are not an exact mirroring of the original representation. This indicates that the margin strongly depends on the data distribution, and it is not solely an effect of the network architecture. Note again that for CIFAR-10 the effect is not as obvious, due to the quite uniform distribution of the margin.

<sup>7</sup>See Sec. B of Supp. material for some visual examples.

### 3.2.2 Invariance and elasticity

The second property we need to verify is that the small margins reported in Fig. 2 do indeed correspond to directions containing discriminative features in the training set. For doing so, we use the insights of Fig. 2(b) on CIFAR-10 – where, opposed to the other datasets, we assume that there are exploited discriminative features in the whole spectrum – and show that, by explicitly modifying its features, we can induce a high margin response in the measured curve in a set of selected directions.

In particular, we create a low-pass filtered version of CIFAR-10 ( $\mathcal{T}_{LP}$ ), where we retain only the frequency components in a  $16 \times 16$  square at the top left of the diagonal of the DCT-transformed images. This way we ensure that no training image has any energy, hence information, outside of this frequency subspace. The median margin<sup>8</sup> of CIFAR-10 test samples for a network trained on  $\mathcal{T}_{LP}$  is illustrated in Fig. 3. Indeed, by eliminating the high frequency content, we have forced the network to become invariant along these directions. This clearly demonstrates that there existed discriminative features in the high frequency spectrum of CIFAR-10, and that by effectively removing these from all the samples, the inductive bias of training pushes the network to become invariant to them.

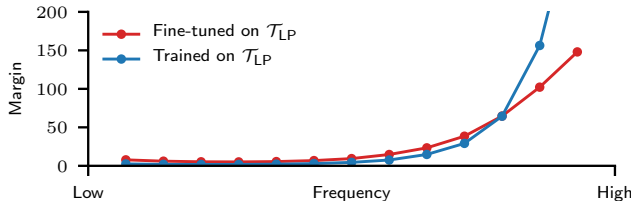


Figure 3: Median margin of test samples from CIFAR-10 for a DenseNet-121 (i) trained on CIFAR-10 and fine-tuned on  $\mathcal{T}_{LP}$  (test: 90.79%), and (ii) trained on  $\mathcal{T}_{LP}$  from scratch (test: 89.67%).

Moreover, this effect can *also* be triggered during training. To show this, we start with the CIFAR-10 trained network studied in Fig. 2(b) and continue training it for a few more epochs with a small learning rate using only  $\mathcal{T}_{LP}$ . Fig. 3 shows the new median margins of this network. The fine-tuned network is again invariant on the high frequencies.

The elasticity to the modification of features during training gives a new perspective to the theory of catastrophic forgetting [32], as it confirms that the decision boundaries of a neural network can only exist for as long as the classifier is trained with the features that hold them together. In Sec. D of Supp. material, we provide an additional experiment to further discuss this relation in which we add and remove points from a dataset, thus triggering an elastic reaction in the network.

Finally, note that by training with only low frequency data, the test accuracy of the network on the original CIFAR-10 only drops around 3%<sup>9</sup>. Because  $\mathcal{T}_{LP}$  has no high frequency energy, a network trained on it will uniformly extend its boundaries in this part of the spectrum and no high frequency perturbation will be able to flip the network’s output. In contrast, testing  $\mathcal{T}_{LP}$  data on a CIFAR-10 trained network only achieves 27.45% test accuracy. This is because networks trained on CIFAR-10 do have boundaries in the high frequencies, and hence showing them original samples perturbed in this frequency range (i.e.,  $\mathcal{T}_{LP}$ ) can greatly change their decisions.

<sup>8</sup>We do not plot the full distribution to avoid clutter. The 5-perc. of the margin in the last subspace is 5.05.

<sup>9</sup>A similar effect was shown on ImageNet [20], although the network was only tested on filtered data.

## 4 Sensitivity to position of training samples

Our novel framework to relate boundary geometry and data features can help track the dynamics of learning. In this section, we use it to explain how training with a slightly perturbed version of the training samples can greatly alter the network geometry. We further analyze how adversarial training can be so successful in removing features with small margin to increase the network’s robustness.

### 4.1 Evidence on synthetic data

We train multiple times an MLP with the same setup as in Section 3.1, but this time using slightly perturbed versions of the same synthetic dataset. In particular, we use a family of training sets  $\mathcal{T}_2(\rho, \epsilon, \sigma, K)$  consisting in  $N = 10,000$  independent  $D = 100$ -dimensional samples  $\mathbf{x}^{(i)} = \mathbf{U}(\mathbf{x}_1^{(i)} \oplus \mathbf{x}_2^{(i)} \oplus \mathbf{x}_3^{(i)})$  such that  $\mathbf{x}_1^{(i)} = \epsilon y^{(i)}$ ;  $\mathbf{x}_2^{(i)} = \rho \cdot k$  when  $y^{(i)} = +1$ , and  $\mathbf{x}_2^{(i)} = \rho \cdot (k + \frac{1}{2})$  when  $y^{(i)} = -1$ , where  $k$  is sampled from a discrete uniform distribution with values  $\{-K, \dots, K-1\}$ ; and  $\mathbf{x}_3^{(i)} \sim \mathcal{N}(0, \sigma^2 \mathbf{I}_{D-2})$  (see Fig. 4). Here,  $\epsilon, \rho \geq 0$  denote the feature sizes. Again, the multiplication by a random orthonormal matrix  $\mathbf{U} \in \text{SO}(D)$  avoids any possible bias of the network towards the canonical basis. Note that for  $\epsilon > 0$  this training set will always be linearly separable using  $\mathbf{u}_1$ , but without necessarily yielding a maximum margin classifier. Especially when  $\rho \gg \epsilon$ .

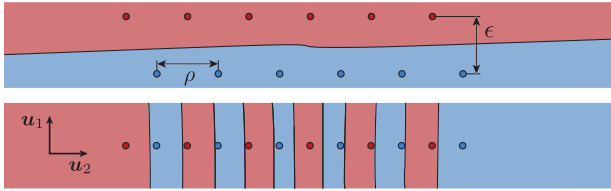


Figure 4: Cross-section of an MLP trained on  $\mathcal{T}_2(\rho = 20, \epsilon, \sigma = 1, K = 3)$  with  $\epsilon = 1$  (**top**) and  $\epsilon = 0$  (**bottom**). Axes scaled differently.

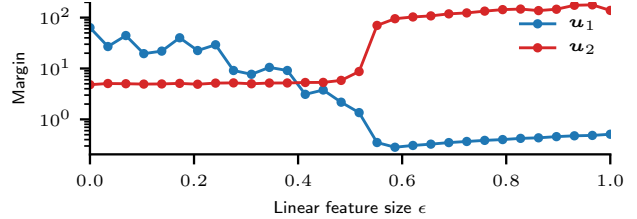


Figure 5: Median margin values along  $\mathbf{u}_1$  and  $\mathbf{u}_2$  for MLPs (test: 100% always) trained on  $\mathcal{T}_2$  for different values of  $\epsilon$  and  $\rho = 20$ .

Fig. 5 shows the median margin values of  $M = 1,000$  observation samples for an MLP trained on different versions of  $\mathcal{T}_2(\rho, \epsilon, \sigma, K)$  with a fixed  $\rho = 20$ , but a varying small  $\epsilon$ . Based on this plot, it is clear that for very small  $\epsilon$  the neural network predominantly uses the information contained in  $\mathbf{u}_2$  to separate the different classes. Indeed, for  $\epsilon < 0.2$ , the network is almost invariant in  $\mathbf{u}_1$ , and it uses a non-linear alternating pattern in  $\mathbf{u}_2$  to separate the data<sup>10</sup> (see bottom row of Fig. 4). On the contrary, at  $\epsilon > 0.5$  we notice a sharp transition in which we see that the neural network suddenly changes its behaviour and starts to linearly separate the different points using only  $\mathbf{u}_1$  (see top row of Fig. 4).

We conjecture that this phenomenon is rooted on the strong inductive bias of the learning algorithm to build connected decision regions whenever geometrically and topologically possible, as empirically validated in [15]. Here, we go one step further and hypothesize that the inductive bias of the learning algorithm has a tendency to build classifiers in which every pair of training samples with the same label belongs to the same decision region. If possible, connected by a straight path.

We see Fig. 5 as a validation of this hypothesis. For small values of  $\epsilon$ , it is hard for the algorithm to find solutions that connect points from the same class with a straight path, as this is very aligned

<sup>10</sup>Note that this particular pattern, can in principle classify any dataset with  $\rho = 20$ , no matter the value of  $\epsilon$ .

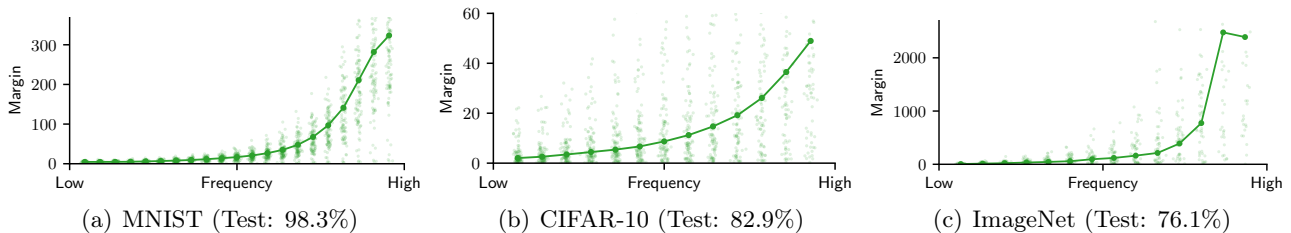


Figure 6: Margin distribution of test samples in subspaces taken from the diagonal of the DCT (low to high frequencies). Adversarially trained networks using  $\ell_2$  PGD [5] (a) LeNet (Adv: 76%), (b) DenseNet-121 (Adv: 55%) and (c) ResNet-50 (Adv: 35%)

with  $\mathbf{u}_2$ . However, there is a precise moment (i.e.,  $\epsilon = 0.5$ ) in which finding such a solution becomes much easier, and then the algorithm suddenly starts to converge to the linearly separating solution.

At this stage it is important to highlight that repeating the same experiment with a different random seed, or for a fixed initialization, does not affect the results. Furthermore, overfitting cannot be the cause of these results, as the MLP always achieves 100% test accuracy for  $\epsilon < 0.5$ , as well. Finally, adding a small weight decay (i.e.,  $10^{-3}$ ) does not help the network find the linearly separable solution for  $\epsilon < 0.5$ ; it rather hinders its convergence (i.e., final train accuracy is 50%).

It remains unclear whether this inductive bias is the only mechanism that can trigger a sharp transition in the type of learned decision boundaries, or if there are other types of biases that can cause the same effect. In any case, we believe that the significant difference in the type of function that the algorithm learns when trained with very similar training samples (see Fig. 4), is an unambiguous confirmation of the sensitivity of deep learning to the exact position of its training input.

## 4.2 Connections to adversarial training

Finally, we show that adversarial training exploits the type of phenomena described in Sec. 4.1 to reshape the boundaries of a neural network. In this regard, Fig. 6 shows the margin distribution across the DCT spectrum of a few adversarially trained networks<sup>11</sup>. As expected, the margins of the adversarially trained networks are significantly higher than those in Fig. 2.

Surprisingly, though, the largest increase can be noticed in the high frequencies for all datasets. Considering that adversarial training only differs from standard training in that it slightly moves the training samples, it is imperative that deep networks converge to very different solutions under such small modifications. The next experiments on CIFAR-10 shed light on the dynamics of this process.

**Adversarial perturbations can trigger invariance in orthogonal directions** Slightly perturbing the training samples can remove features in an unpredictable manner. Fig. 7 shows the spectral decomposition of the adversarial perturbations crafted during adversarial training of CIFAR-10. The energy of the perturbations during training is always concentrated in the low frequencies, and has hardly any high frequency content. However, the greatest effect on margin is seen on the orthogonal high frequency directions (see Fig. 6). This is similar to what seen in Fig. 4, where slightly perturbing the training samples along  $\mathbf{u}_1$  drastically affects the margin along  $\mathbf{u}_2$ .

<sup>11</sup>The analogous effect for the “flipped” datasets (cf. Section 3.2.1) is detailed in Sec. M of Supp. material.

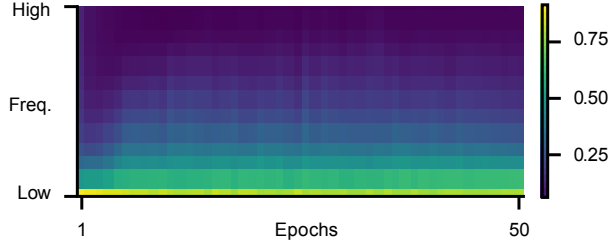


Figure 7: Energy of adversarial perturbations on subspaces of the DCT during adv. training of CIFAR-10 (DenseNet-121). Plot shows 95-perc.

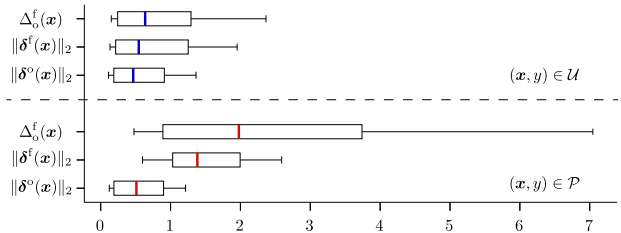


Figure 8: Margin distribution in different directions of a ResNet-18 trained on CIFAR-10 and fine-tuned on 100 DeepFool examples.

Overall, we see that adversarial training exploits the sensitivity of the network to small changes in the training samples to hide some discriminative features from the model. This is especially clear when we compare the CIFAR-10 values in Fig. 6(b) and Fig. 2(b), where it becomes evident that some previously used discriminative features in the high frequencies are completely overlooked by the adversarially trained network. In the following example, we show that, in practice, it is not actually necessary to change the position of all training points to induce a large invariance reaction.

**Invariance can be triggered by just a few samples** Modifying the position of just a *minimal* number of training samples is enough to locally introduce excessive invariance on a classifier. To demonstrate this, we take a ResNet-18 (test: 89%) trained on CIFAR-10, and randomly select a set of 100 training samples  $\mathcal{P} \subset \mathcal{T}$ . We fine-tune this classifier replacing those 100 samples with  $(\mathbf{x} + \delta^o(\mathbf{x}), y)$  in  $\mathcal{P}$  (test: 90%), where  $\delta^o$  and  $\delta^f$  represent the adversarial perturbations for the original and fine-tuned network, respectively.

Fig. 8 shows the magnitude of these perturbations both for the 100 adversarially perturbed points  $\mathcal{P} \subset \mathcal{T}$  and for a subset of 1,000 unmodified samples  $\mathcal{U} \subset \mathcal{T}$ . Here, we can clearly see that, after fine-tuning, the boundaries around  $\mathcal{P}$  have been completely modified, showing a large increase in the distance to the boundary in the direction of the original adversarial perturbation  $\Delta_0^f(\mathbf{x})$  for  $(\mathbf{x}, y) \in \mathcal{P}$ . Meanwhile, the boundaries around  $\mathcal{U}$  have not seen such a dramatic change.

This means that modifying the position of *only* a small fraction of the training samples can induce a large change in the shape of the boundary. Note that this dependency on a few samples resembles the one of support vector machines [33], whose decision boundaries are defined by the position of a few supporting vectors. However, in contrast to SVMs, deep neural networks are not guaranteed to maximize margin in the input space (see Fig. 5) and the points that support their boundaries need not be the ones closest to them, hence rendering their identification much harder.

## 5 Concluding remarks

In this paper, we proposed a new framework that permits to relate data features and margin along specific directions. We also explained how the inductive bias of the learning algorithm shapes the decision boundaries of neural networks by creating boundaries that are invariant to non-discriminative directions. We further showed that these boundaries are very sensitive to the exact position of the training samples, and that this enables adversarial training to build more robust classifiers.

**Future directions** We believe that our new framework can be used in future research to investigate the connections between training features and the macroscopic geometry of deep models. This can serve as a tool to obtain new insights on the intriguing properties of deep networks such as their catastrophic forgetting [32]. On the practical side, there are some important applications that could benefit from our findings. In terms of robustness, identifying the small subspace of discriminative features of a network can lead to faster black box-attacks by restricting the search space of the perturbations. In fact our analysis explains why in recent attacks [7, 21, 34] using low-frequency perturbations improves the query efficiency. Simultaneously, the dependency of boundaries to just a few training samples can be exploited to design faster adversarial training schemes, and is a clear avenue for future research in active learning [35]. Finally, having a better understanding about the mechanisms that lead to excessive invariance [14] after adversarial training could help boost the standard accuracy of robust models.

## Broader impact

In this work, we build on the mechanisms of adversarial machine learning and propose a new framework that connects the microscopic features of a dataset (i.e., position of the training samples in the input space) to the macroscopic properties of the learned models (e.g., distance to the decision boundary). Our methodology sheds light onto the inductive bias that deep classifiers exploit for shaping their decision boundaries and might explain the successes and limitations of deep learning.

Part of our work continues a recent line of research that shows that the way neural networks perceive the image spectrum is very different to the way humans do. In fact, based on the margin distributions for different frequencies that we measure, we can see that neural networks can sometimes use features in the higher end of the spectrum which are invisible to the human eye (see Fig. 2 and [4, 20]). A positive application of our work would therefore be the use of this knowledge and some methods derived from our experimental framework to better align the behavior of neural networks to the human visual system perception. This could have positive implications in the interpretability of neural networks when deployed on some domains where it is necessary to explain the decisions of a classifier, e.g., medical imaging.

We see the main possible negative implication of our work in the malicious exploitation of the discriminative features of the datasets for generating more advanced and efficient adversarial attacks. When deploying deep models into the real world, especially for safety-critical applications, it is of high importance that practitioners are aware of the low margin blindspots in the classifiers and make the best to protect them.

## Acknowledgments

We thank Maksym Andriushchenko, and Evangelos Alexiou for their fruitful discussions and feedback. This work has been partially supported by the CHIST-ERA program under Swiss NSF Grant 20CH21\_180444, and partially by Google via a Postdoctoral Fellowship and a GCP Research Credit Award.

## References

- [1] C. Szegedy, W. Zaremba, I. Sutskever, J. Bruna, D. Erhan, I. J. Goodfellow, and R. Fergus, “Intriguing properties of neural networks,” in *International Conference on Learning Representations (ICLR 2014)*, 2014.
- [2] I. J. Goodfellow, J. Shlens, and C. Szegedy, “Explaining and harnessing adversarial examples,” in *International Conference on Learning Representations (ICLR 2015)*, 2015.
- [3] S. Jetley, N. A. Lord, and P. H. S. Torr, “With Friends Like These, Who Needs Adversaries?,” in *Advances in Neural Information Processing Systems (NeurIPS 2018)*, pp. 10749–10759, Curran Associates, Inc., 2018.
- [4] A. Ilyas, S. Santurkar, D. Tsipras, L. Engstrom, B. Tran, and A. Madry, “Adversarial Examples Are Not Bugs, They Are Features,” in *Advances in Neural Information Processing Systems (NeurIPS 2019)*, pp. 125–136, Curran Associates, Inc., 2019.
- [5] A. Madry, A. Makelov, L. Schmidt, D. Tsipras, and A. Vladu, “Towards Deep Learning Models Resistant to Adversarial Attacks,” in *International Conference on Learning Representations (ICLR 2018)*, 2018.
- [6] S.-M. Moosavi-Dezfooli, A. Fawzi, J. Uesato, and P. Frossard, “Robustness via Curvature Regularization, and Vice Versa,” in *IEEE Conference on Computer Vision and Pattern Recognition (CVPR 2019)*, pp. 9070–9078, IEEE, 2019.
- [7] Y. Sharma, G. W. Ding, and M. A. Brubaker, “On the Effectiveness of Low Frequency Perturbations,” in *International Joint Conference on Artificial Intelligence (IJCAI 2019)*, pp. 3389–3396, International Joint Conferences on Artificial Intelligence Organization, 2019.
- [8] C. Zhang, S. Bengio, M. Hardt, B. Recht, and O. Vinyals, “Understanding deep learning requires rethinking generalization,” in *International Conference on Learning Representations (ICLR 2017)*, 2017.
- [9] S. Gunasekar, J. Lee, D. Soudry, and N. Srebro, “Characterizing Implicit Bias in Terms of Optimization Geometry,” in *Proceedings of the 35th International Conference on Machine Learning (ICML 2018)*, pp. 1832–1841, PMLR, 2018.
- [10] M. Belkin, D. Hsu, S. Ma, and S. Mandal, “Reconciling modern machine-learning practice and the classical bias–variance trade-off,” *Proceedings of the National Academy of Sciences*, vol. 116, no. 32, pp. 15849–15854, 2019.
- [11] D. Soudry, E. Hoffer, M. S. Nacson, S. Gunasekar, and N. Srebro, “The Implicit Bias of Gradient Descent on Separable Data,” in *International Conference on Learning Representations (ICLR 2018)*, 2018.
- [12] Y. Li, L. Ding, and X. Gao, “On the Decision Boundary of Deep Neural Networks,” *arXiv:1808.05385*, Aug. 2018.
- [13] S. Santurkar, D. Tsipras, B. Tran, A. Ilyas, L. Engstrom, and A. Madry, “Image Synthesis with a Single (Robust) Classifier,” in *Advances in Neural Information Processing Systems (NeurIPS 2019)*, pp. 1260–1271, Curran Associates, Inc., 2019.

- [14] F. Tramér, J. Behrmann, N. Carlini, N. Papernot, and J.-H. Jacobsen, “Fundamental tradeoffs between invariance and sensitivity to adversarial perturbations,” *arXiv:2002.04599*, 2020.
- [15] A. Fawzi, S.-M. Moosavi-Dezfooli, P. Frossard, and S. Soatto, “Empirical Study of the Topology and Geometry of Deep Networks,” in *IEEE Conference on Computer Vision and Pattern Recognition (CVPR 2018)*, pp. 3762–3770, IEEE, 2018.
- [16] K. N. Ramamurthy, K. R. Varshney, and K. Mody, “Topological Data Analysis of Decision Boundaries with Application to Model Selection,” in *Proceedings of the 36th International Conference on Machine Learning (ICML 2019)*, pp. 5351–5360, PMLR, 2019.
- [17] W. He, B. Li, and D. Song, “Decision Boundary Analysis of Adversarial Examples,” in *International Conference on Learning Representations (ICLR 2018)*, 2018.
- [18] G. Elsayed, D. Krishnan, H. Mobahi, K. Regan, and S. Bengio, “Large Margin Deep Networks for Classification,” in *Advances in Neural Information Processing Systems (NeurIPS 2018)*, pp. 842–852, Curran Associates, Inc., 2018.
- [19] Y. Jiang, D. Krishnan, H. Mobahi, and S. Bengio, “Predicting the Generalization Gap in Deep Networks with Margin Distributions,” in *International Conference on Learning Representations (ICLR 2019)*, 2019.
- [20] D. Yin, R. G. Lopes, J. Shlens, E. D. Cubuk, and J. Gilmer, “A Fourier Perspective on Model Robustness in Computer Vision,” in *Advances in Neural Information Processing Systems (NeurIPS 2019)*, pp. 13255–13265, Curran Associates, Inc., 2019.
- [21] Y. Tsuzuku and I. Sato, “On the Structural Sensitivity of Deep Convolutional Networks to the Directions of Fourier Basis Functions,” in *IEEE Conference on Computer Vision and Pattern Recognition (CVPR 2019)*, pp. 51–60, IEEE, 2019.
- [22] S.-M. Moosavi-Dezfooli, A. Fawzi, and P. Frossard, “DeepFool: A Simple and Accurate Method to Fool Deep Neural Networks,” in *IEEE Conference on Computer Vision and Pattern Recognition (CVPR 2016)*, pp. 2574–2582, IEEE, 2016.
- [23] A. Fawzi, S.-M. Moosavi-Dezfooli, and P. Frossard, “The Robustness of Deep Networks: A Geometrical Perspective,” *IEEE Signal Processing Magazine*, vol. 34, no. 6, pp. 50–62, 2017.
- [24] Y. Lecun, L. Bottou, Y. Bengio, and P. Haffner, “Gradient-based learning applied to document recognition,” *Proceedings of the IEEE*, vol. 86, no. 11, pp. 2278–2324, 1998.
- [25] A. Krizhevsky, “Learning Multiple Layers of Features from Tiny Images,” tech. rep., University of Toronto, 2009.
- [26] J. Deng, W. Dong, R. Socher, L. J. Li, L. Kai, and F. F. Li, “ImageNet: A large-scale hierarchical image database,” in *IEEE Conference on Computer Vision and Pattern Recognition (CVPR 2009)*, pp. 248–255, IEEE, 2009.
- [27] A. Paszke, S. Gross, F. Massa, A. Lerer, J. Bradbury, G. Chanan, T. Killeen, Z. Lin, N. Gimelshein, L. Antiga, A. Desmaison, A. Kopf, E. Yang, Z. DeVito, M. Raison, A. Tejani, S. Chilamkurthy, B. Steiner, L. Fang, J. Bai, and S. Chintala, “PyTorch: An Imperative

- Style, High-Performance Deep Learning Library,” in *Advances in Neural Information Processing Systems (NeurIPS 2019)*, pp. 8024–8035, Curran Associates, Inc., 2019.
- [28] N. Ahmed, T. Natarajan, and K. R. Rao, “Discrete Cosine Transform,” *IEEE Transactions on Computers*, vol. C-23, no. 1, pp. 90–93, 1974.
  - [29] G. Huang, Z. Liu, L. Van Der Maaten, and K. Q. Weinberger, “Densely connected convolutional networks,” in *IEEE Conference on Computer Vision and Pattern Recognition (CVPR 2017)*, pp. 2261–2269, IEEE, 2017.
  - [30] K. He, X. Zhang, S. Ren, and J. Sun, “Deep residual learning for image recognition,” in *IEEE Conference on Computer Vision and Pattern Recognition (CVPR 2016)*, pp. 770–778, IEEE, 2016.
  - [31] F. W. Campbell and J. G. Robson, “Application of fourier analysis to the visibility of gratings,” *The Journal of Physiology*, vol. 197, no. 3, pp. 551–566, 1968.
  - [32] M. McCloskey and N. J. Cohen, “Catastrophic Interference in Connectionist Networks: The Sequential Learning Problem,” *Psychology of Learning and Motivation*, vol. 24, pp. 109–165, 1989.
  - [33] C. Cortes and V. Vapnik, “Support-vector networks,” *Machine Learning*, vol. 20, no. 3, pp. 273–297, 1995.
  - [34] A. Rahmati, S.-M. Moosavi-Dezfooli, P. Frossard, and H. Dai, “GeoDA: a geometric framework for black-box adversarial attacks,” *arXiv:2003.06468*, Mar. 2020.
  - [35] L. E. Atlas, D. A. Cohn, and R. E. Ladner, “Training Connectionist Networks with Queries and Selective Sampling,” in *Advances in Neural Information Processing Systems (NeurIPS)*, pp. 566–573, Morgan-Kaufmann, 1990.
  - [36] V. Nagarajan and J. Z. Kolter, “Uniform convergence may be unable to explain generalization in deep learning,” in *Advances in Neural Information Processing Systems (NeurIPS 2019)*, pp. 11611–11622, Curran Associates, Inc., 2019.
  - [37] L. Engstrom, A. Ilyas, S. Santurkar, and D. Tsipras, “Robustness (python library),” 2019.
  - [38] J. P. Boyle and R. L. Dykstra, “A method for finding projections onto the intersection of convex sets in hilbert spaces,” in *Advances in Order Restricted Statistical Inference*, pp. 28–47, Springer New York, 1986.
  - [39] A. Fawzi, S. M. Moosavi-Dezfooli, and P. Frossard, “Robustness of classifiers: From adversarial to random noise,” in *Advances in Neural Information Processing Systems (NeurIPS 2016)*, pp. 1632–1640, Curran Associates, Inc, 2016.

## A Theoretical margin distribution of a linear classifier

In this section we prove that even for linear classifiers trained on  $\mathcal{T}_1(\epsilon, \rho, N)$  the distribution of margins along non-discriminative directions will never be infinite, and that it will have a large variance (c.f. Section 3.1). This effect is due to the finiteness of the training set which boosts the influence of the non-discriminative directions in the final solution of the optimization. In particular, we show this for the linear classifier introduced in [36] and prove the following proposition:

**Proposition.** *Let  $f(\mathbf{x}) = \mathbf{w}^T \mathbf{x}$  be a linear classifier trained on  $\mathcal{T}_1(\epsilon, \sigma, N)$  using one-step gradient descent initialized with  $\mathbf{w} = 0$  and  $\alpha = 1$  to maximize  $f(\mathbf{x}^{(i)})y^{(i)}$  for every sample, and let  $\xi^2(\mathbf{x})$  denote the ratio between the margin in the direction of the discriminative feature  $\text{span}\{\mathbf{u}_1\}$  and the margin in an orthogonal random subspace  $\mathcal{S}_{\text{orth}} \subseteq \text{span}\{\mathbf{u}_1\}^\perp$  of dimension  $|\mathcal{S}| = S \leq D - 1$ , i.e.,*

$$\xi^2(\mathbf{x}) = \frac{\|\delta_{\mathbf{u}_1}(\mathbf{x})\|_2^2}{\|\delta_{\mathcal{S}_{\text{orth}}}(\mathbf{x})\|_2^2}.$$

*The distribution of  $\xi^2(\mathbf{x})$  is independent of  $\mathbf{x}$  and follows  $\xi^2(\mathbf{x}) \sim N\sigma^2\chi_S^2$ , where  $\chi_S^2$  denotes the Chi-squared distribution with  $S$  degrees of freedom. In particular,*

$$\text{median}(\xi^2) = \mathcal{O}\left(\frac{\sigma^2}{N\epsilon^2}S\right) \quad \text{and} \quad \text{Var}(\xi^2) = \frac{2\sigma^4}{N^2\epsilon^4}S$$

*Proof.* First, note that the weights of the classifier, after one step of GD, are

$$\mathbf{w} = \nabla_{\mathbf{w}} \sum_{i=0}^{N-1} f(\mathbf{x}^{(i)})y^{(i)} = \sum_{i=0}^{N-1} \mathbf{x}^{(i)}y^{(i)} = \mathbf{U} \sum_{i=0}^{N-1} (\mathbf{x}_1^{(i)} \oplus \mathbf{x}_2^{(i)})y^{(i)}.$$

Hence,

$$\mathbf{w} = \mathbf{U}(\mathbf{w}_1 \oplus \mathbf{w}_2) \quad \text{with} \quad \begin{cases} \mathbf{w}_1 = \sum_{i=0}^{N-1} y^{(i)} \mathbf{x}_1^{(i)} = N\epsilon \\ \mathbf{w}_2 = \sum_{i=0}^{N-1} y^{(i)} \mathbf{x}_2^{(i)} \end{cases}$$

Since  $y^{(i)}$  are uniform discrete random variables taking values from  $\{-1, +1\}$ ,  $\mathbf{x}_2^{(i)}$  are standard normal random variables independent from  $y^{(i)}$ , it can be shown that their product  $y^{(i)}\mathbf{x}_2^{(i)}$  is also a standard normal random variable. Hence,  $\mathbf{w}_2 \sim \mathcal{N}(0, N\sigma^2 \mathbf{I}_{D-1})$ .

Recall that for linear classifiers the distance to the decision boundary of a point  $\mathbf{x}$  on a vector subspace  $\mathcal{S} \subseteq \mathbb{R}^D$  can be computed in closed form as

$$\|\delta_{\mathcal{S}}(\mathbf{x})\|_2 = \frac{|\mathbf{w}^T \mathbf{x}|}{\|\mathcal{P}_{\mathcal{S}}(\mathbf{w})\|_2}$$

where  $\mathcal{P}_{\mathcal{S}} : \mathbb{R}^D \rightarrow \mathbb{R}^D$  denotes the orthogonal projection operator onto the subspace  $\mathcal{S}$ . Considering this, we can compute both the margin in  $\text{span}\{\mathbf{u}_1\}$  and  $\mathcal{S}_{\text{orth}}$  as

$$\begin{aligned} \|\delta_{\text{span}\{\mathbf{u}_1\}}(\mathbf{x})\|_2 &= \frac{|\mathbf{w}^T \mathbf{x}|}{\|\mathcal{P}_{\text{span}\{\mathbf{u}_1\}}(\mathbf{w})\|_2} = \frac{|\mathbf{w}^T \mathbf{x}|}{\|\mathbf{w}_1\|_2}, \\ \|\delta_{\mathcal{S}_{\text{orth}}}(\mathbf{x})\|_2 &= \frac{|\mathbf{w}^T \mathbf{x}|}{\|\mathcal{P}_{\mathcal{S}_{\text{orth}}}(\mathbf{w})\|_2} = \frac{|\mathbf{w}^T \mathbf{x}|}{\|\mathcal{P}_{\mathcal{S}_{\text{orth}}}^{D-1}(\mathbf{w}_2)\|_2}, \end{aligned}$$

where  $\mathcal{S}_{\text{orth}}^{D-1} \subseteq \mathbb{R}^{D-1}$  is the subspace generated by the last  $D - 1$  components of the vectors in  $\mathcal{S}$ .

Squaring these distances and taking their ratio we have

$$\xi^2 = \frac{\|\delta_{\text{span}\{\mathbf{u}_1\}}(\mathbf{x})\|_2^2}{\|\delta_{\mathcal{S}_{\text{orth}}}(\mathbf{x})\|_2^2} = \frac{\|\mathcal{P}_{\mathcal{S}_{\text{orth}}^{D-1}}(\mathbf{w}_2)\|_2^2}{\|\mathbf{w}_1\|_2^2}.$$

Note now that due to the rotational symmetry of  $\mathcal{N}(0, \mathbf{I}_{D-1})$

$$\mathcal{P}_{\mathcal{S}_{\text{orth}}^{D-1}}(\mathbf{w}_2) \sim \mathcal{N}\left(0, N\sigma^2 \mathbf{U}_{\mathcal{S}_{\text{orth}}^{D-1}} \mathbf{I}_S \mathbf{U}_{\mathcal{S}_{\text{orth}}^{D-1}}^T\right),$$

where  $\mathbf{U}_{\mathcal{S}_{\text{orth}}^{D-1}} \in \mathbb{R}^{D-1 \times S}$  is a matrix whose columns form an orthonormal basis of  $\mathcal{S}_{\text{orth}}^{D-1}$ . Hence,  $\|\mathcal{P}_{\mathcal{S}_{\text{orth}}^{D-1}}(\mathbf{w}_2)\|_2^2 \sim N\sigma^2 \chi_S^2$  and

$$\xi^2 = \frac{\|\mathcal{P}_{\mathcal{S}_{\text{orth}}^{D-1}}(\mathbf{w}_2)\|_2^2}{\|\mathbf{w}_1\|_2^2} = \frac{\|\mathcal{P}_{\mathcal{S}_{\text{orth}}^{D-1}}(\mathbf{w}_2)\|_2^2}{N^2 \epsilon^2} \sim \frac{\sigma^2}{N \epsilon^2} \chi_S^2.$$

Finally, plugging in the expression for the median and variance of a Chi-squared distribution we get

$$\text{median}(\xi^2) \approx \frac{\sigma^2}{N \epsilon^2} S \left(1 - \frac{2}{9S}\right)^3,$$

and

$$\text{Var}(\xi^2) = \frac{2\sigma^4}{N^2 \epsilon^4} S.$$

□

Clearly,  $\text{median}(\xi^2)$  decreases asymptotically with respect to the number of samples. Nevertheless, due to the finiteness of the training set, small but non-zero values of  $\xi^2$  are unavoidable. Similarly,  $\text{Var}(\xi^2)$  only decreases quadratically with the number of samples and grows linearly with the dimensionality of  $\mathcal{S}_{\text{orth}}$ . Hence, some fluctuations in the measured margins are expected even for linear classifiers.

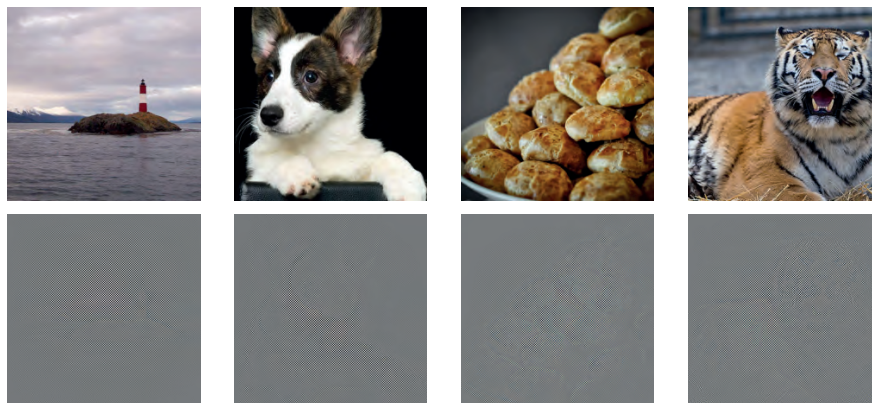
We demonstrate this effect in practice by repeating the experiment of Sec. 3.1, where instead of an MLP we use a simple logistic regression (see Table 2). Clearly, although the values along  $\text{span}\{\mathbf{u}_1\}^\perp$  are quite large, they are still finite. This demonstrates that due to the finiteness of the training set and its high-dimensionality the influence of the non-discriminative directions in the final solution is significant.

Table 2: Margin statistics of a logistic regressor trained on  $\mathcal{T}_1(\epsilon = 5, \sigma = 1)$  along different directions ( $N = 10,000$ ,  $M = 1,000$ ,  $S = 3$ ).

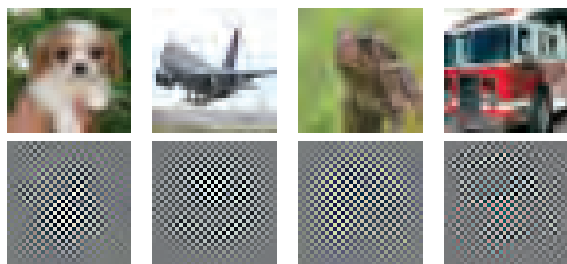
	$\mathbf{u}_1$	$\text{span}\{\mathbf{u}_1\}^\perp$	$\mathcal{S}_{\text{ORTH}}$	$\mathcal{S}_{\text{RAND}}$
5-PERC.	2.39	36.7	184.95	11.57
MEDIAN	2.49	38.3	192.98	12.08
95-PERC.	2.60	39.92	201.16	12.59

## B Examples of frequency “flipped” images

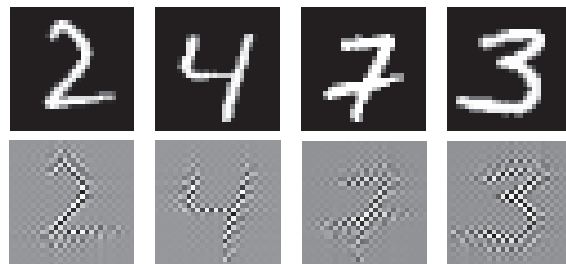
Figure 9 shows a few example images of the frequency “flipped” versions of the standard computer vision datasets.



(a) ImageNet



(b) CIFAR-10



(c) MNIST

Figure 9: “Flipped” image examples. **Top** rows show original images and **bottom** rows the “flipped” versions.

## C Invariance and elasticity on MNIST data

We further validate our observation of Section 3.2.2 that small margin do indeed corresponds to directions containing discriminative features in the training set, but this time for a different dataset (MNIST), on a different network (ResNet-18), and using different discriminative features (high-frequency). In particular, we create a high-pass filtered version of MNIST ( $\text{MNIST}_{\text{HP}}$ ), where we completely remove the frequency components in a  $14 \times 14$  square at the top left of the diagonal of the DCT-transformed images. This way we ensure that every pairwise connection between the training images (features) has zero components outside of this frequency subspace. The margin distribution of 1,000 MNIST test samples for a ResNet-18 trained on  $\text{MNIST}_{\text{HP}}$  is illustrated in Figure 10. Indeed, similarly to the observations on CIFAR-10, by eliminating the low frequency features, we have forced an increased margin along these directions, while forcing the network to focus on the previously unused high frequency features.

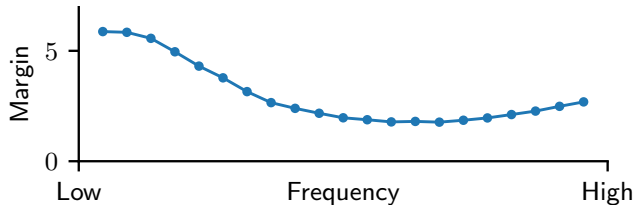


Figure 10: Median margin of test samples from MNIST for a ResNet-18 trained on  $\text{MNIST}_{\text{HP}}$  from scratch (test: 98.71%).

## D Connections to catastrophic forgetting

The elasticity to the modification of features during training gives a new perspective to the theory of catastrophic forgetting [32], as it confirms that the decision boundaries of a neural network can only exist for as long as the classifier is trained with the samples (features) that hold them together. In particular, we demonstrate this by adding and removing points from a dataset such that its discriminative features are modified during training, and hence artificially causing an elastic response on the network.

To this end, we train a DenseNet-121 on a new dataset  $\mathcal{T}_{\text{LP} \cup \text{HP}} = \mathcal{T}_{\text{LP}} \cup \mathcal{T}_{\text{HP}}$  formed by the union of two filtered variants of CIFAR-10:  $\mathcal{T}_{\text{LP}}$  is constructed by retaining only the frequency components in a  $16 \times 16$  square at the top-left of the DCT-transformed CIFAR-10 images (low-pass), while for  $\mathcal{T}_{\text{HP}}$  only the frequency components in a  $16 \times 16$  square at the bottom-right of the DCT (high-pass). This classifier has a test accuracy of 86.59% and 57.29% on  $\mathcal{T}_{\text{LP}}$  and  $\mathcal{T}_{\text{HP}}$ , respectively. The median margin of 1,000  $\mathcal{T}_{\text{LP}}$  test samples along different frequencies for this classifier is shown in blue in Figure 11. As expected, the classifier has picked features across the whole spectrum with the low frequency ones probably belonging to boundaries separating samples in  $\mathcal{T}_{\text{LP}}$ , and the high frequency ones separating samples from  $\mathcal{T}_{\text{LP}}$  and  $\mathcal{T}_{\text{HP}}$ <sup>12</sup>.

<sup>12</sup> $\mathcal{T}_{\text{LP}}$  and  $\mathcal{T}_{\text{HP}}$  have only discriminative features in the low-frequency and high-frequency part of the spectrum, respectively.

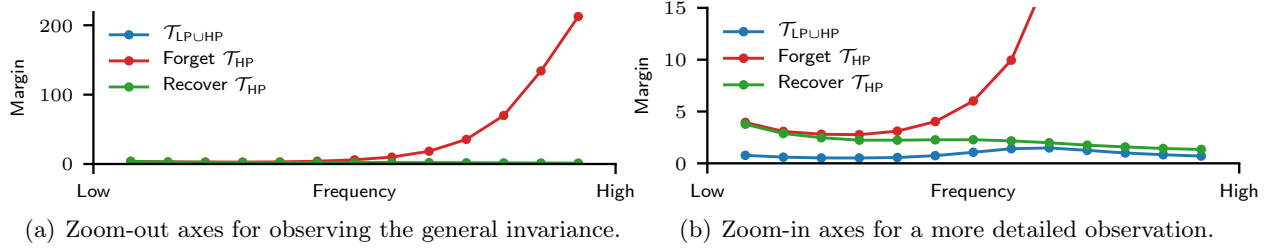


Figure 11: Median margin of  $\mathcal{T}_{LP}$  test samples for a DenseNet-121. **Blue:** trained on  $\mathcal{T}_{LP \cup HP}$ ; **Red:** after forgetting  $\mathcal{T}_{HP}$ ; **Green:** after recovering  $\mathcal{T}_{HP}$ .

After this, we continue training the network with a linearly decaying learning rate (max.  $\alpha = 0.05$ ) for another 30 epochs, but using only  $\mathcal{T}_{LP}$ , achieving a final test accuracy of 87.81% and 10.01% on  $\mathcal{T}_{LP}$  and  $\mathcal{T}_{HP}$ , respectively. Again, Figure 11 shows in red the median margin along different frequencies on test samples from  $\mathcal{T}_{LP}$ . The new median margin is clearly invariant on the high frequencies – where  $\mathcal{T}_{LP}$  has no discriminative features – and the classifier has completely *erased* the boundaries that it previously had in these regions, regardless of the fact that those boundaries did not harm the classification accuracy on  $\mathcal{T}_{LP}$ .

Finally, we investigate if the network is able to recover the forgotten decision boundaries that were used to classify  $\mathcal{T}_{HP}$ . We continue training the network (“forgotten”  $\mathcal{T}_{HP}$ ) for another 30 epochs, but this time by using the whole  $\mathcal{T}_{LP \cup HP}$ . Now this classifier achieves a final test accuracy of 86.1% and 59.11% on  $\mathcal{T}_{LP}$  and  $\mathcal{T}_{HP}$  respectively, which are very close to the corresponding accuracies of the initial network trained from scratch on  $\mathcal{T}_{LP \cup HP}$  (recall: 86.59% and 57.29%). The new median margin for this classifier is shown in green in Figure 11. As we can see by comparing the green to the blue curve, the decision boundaries along the high-frequency directions can be recovered quite successfully.

## E Examples of filtered images

Figure 12 shows a few example images of the filtered versions of the standard computer vision datasets used in the Section 3.2.2, C and D.

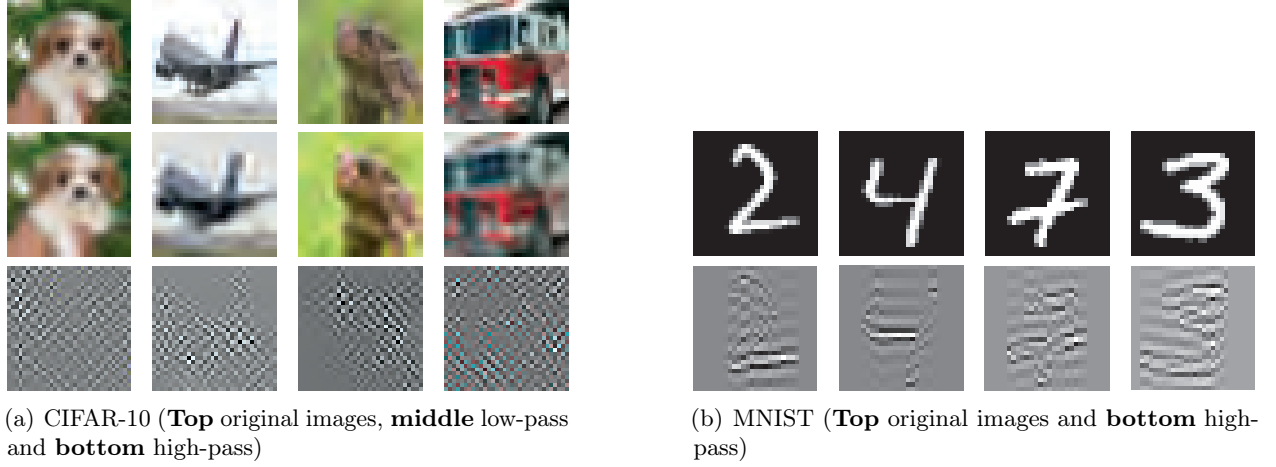


Figure 12: Filtered image examples.

## F Subspace sampling of the DCT

In most of our experiments with real data we measured the margin of  $M$  samples on a sequence of subspaces created using blocks from the DCT. In particular, we use a sequence of  $K \times K$  blocks sampled from the DCT tensor either from a sliding window on the diagonal with step size  $T$  or a grid with stride  $T$  (c.f. Figure 13).

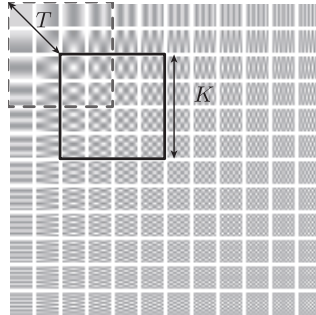


Figure 13: Diagram illustrating the main parameters defining the subspace sequence from the diagonal of the DCT.

## G Training parameters

Table 3 shows the performance and training parameters of the different networks used in the paper. Note that the hyperparameters of these networks were not optimized in any form during this work. Instead they were selected from a set of best practices from the DAWNBench submissions that have been empirically shown to give a good trade-off in terms of convergence speed and performance. In this sense, especially for the non-standard datasets (e.g., “flipped” datasets), the final performance might not be the best reflection of the highest achievable performance of a given architecture. In fact, since the goal of our experiments is not to achieve the most robust models on such non-standard datasets, but rather investigate how the previously observed trends are represented in these new classifiers, no further hyperparameter tuning was applied.

Table 3: Performance and training parameters of multiple networks trained on different datasets. All networks have been trained using SGD with momentum 0.9 and a weight decay of  $5 \times 10^{-4}$ . For ImageNet, the training parameters are not known, since we use the pretrained models from PyTorch. For “flipped” ImageNet, the weight decay was set to  $10^{-4}$ , while for computational reasons the training was executed until the 68<sup>th</sup> epoch.

DATASET	NETWORK	TEST ACC.	EPOCHS	LR SCHEDULE	MAX. LR	BATCH
MNIST	LeNET	99.35%	30	TRIANG.	0.21	128
	RESNET-18	99.53%				
MNIST FLIPPED	LeNET RESNET-18	99.34% 99.52%	30	TRIANG.	0.21	128
CIFAR-10	VGG-19	89.39%	50	TRIANG.	0.21	128
	RESNET-18	90.05%				
	DENSENET-121	93.03%				
CIFAR-10 LOW PASS	VGG-19	84.81%	50	TRIANG.	0.21	128
	RESNET-18	84.77%				
	DENSENET-121	93.03%				
CIFAR-10 FLIPPED	VGG-19	87.42%	50	TRIANG.	0.21	128
	RESNET-18	88.67%				
	DENSENET-121	88.51%				
IMAGENET	VGG-16	71.59%	—	—	—	—
	RESNET-50	76.15%				
	DENSENET-121	74.65%				
IMAGENET FLIPPED	RESNET-50	68.12%	90(68)	PIECEWISE CONSTANT	0.1	256

As mentioned in the paper, all the experiments with synthetic data were trained in the same way, namely using SGD with a linearly decaying learning rate (max lr. 0.1), no explicit regularization,

and trained for 500 epochs.

## H Cross-dataset performance

We now show the performance of different networks trained with different variants of the standard computer vision datasets and tested on the rest.

Table 4: Multiple networks trained on a specific version of MNIST, but evaluated on different variations of it. Rows denote the dataset that each network is trained on, and columns the dataset they are evaluated on. Values on the diagonal correspond to the same variation.

		MNIST	MNIST FLIPPED	MNIST HIGH PASS
MNIST	LeNET	99.35%	18.73%	44.09%
	RESNET-18	99.53%	11.88%	15.73%
MNIST	LeNET	10.52%	99.34%	9.87%
FLIPPED	RESNET-18	16.59%	99.52%	11.23%
MNIST	LeNET	96.35%	42.36%	98.65%
HIGH PASS	RESNET-18	88.38%	21.48%	98.71%

Table 5: Multiple networks trained on a specific version of CIFAR-10, but evaluated on different variations of it. Rows denote the dataset that each network is trained on, and columns the dataset they are evaluated on. Values on the diagonal correspond to the same variation.

		CIFAR-10	CIFAR-10 FLIPPED	CIFAR-10 LOW PASS
CIFAR-10	VGG-19	89.39%	10.63%	61.4%
	RESNET-18	90.05%	10%	46.99%
	DENSENET-121	93.03%	10.3%	27.45%
CIFAR-10	VGG-19	10.77%	87.42%	10.79%
FLIPPED	RESNET-18	9.91%	88.67%	9.97%
	DENSENET-121	9.98%	88.51%	10%
CIFAR-10	VGG-19	85.16%	10.52%	84.81%
LOW PASS	RESNET-18	85.47%	10.45%	84.77%
	DENSENET-121	89.67%	10.45%	88.51%

Table 6: Multiple networks trained on a specific version of ImageNet, but evaluated on different variations of it. Rows denote the dataset that each network is trained on, and columns the dataset they are evaluated on. Values on the diagonal correspond to the same variation.

		IMAGENET	IMAGENET FLIPPED
IMAGENET	VGG-16	71.59%	0.106%
	RESNET-50	76.15%	0.292%
	DENSENET-121	74.65%	0.22%
IMAGENET FLIPPED	RESNET-50	0.184%	68.12%

## I Margin distribution for standard networks

We show here the margin distribution on the diagonal of the DCT for different networks trained using multiple datasets using the setup specified in Section G. We also show the median margin for the same  $M$  samples on a grid from the DCT.

The first thing to notice is that, for a given dataset, the trend of the margins are quite similar regardless the network architecture. Also, regardless the evaluation (diagonal or grid), the observed margins between train and test samples are very similar, with the differences in the values being quite minimal. Furthermore, for the grid evaluations, the trend of the median margins with respect to subspaces of different frequencies (increasing from low to high frequencies) is similar to the corresponding one of the diagonal evaluations. Hence, the choice of the diagonal of the DCT is sufficient for measuring the margin along directions of the frequency spectrum. Finally, in every evaluation (diagonal or grid) and for every data set (train or test), “flipping” the representation of the data results in “flipped” margins as well, with CIFAR-10 results being an exception due to the quite uniform distribution of the margin across the whole frequency spectrum.

## I.1 MNIST

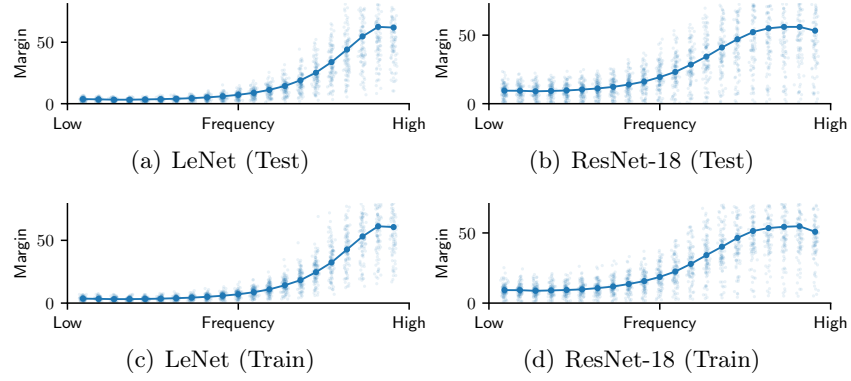


Figure 14: Diagonal **MNIST** ( $M = 1,000$ ,  $K = 8$ ,  $T = 1$ )

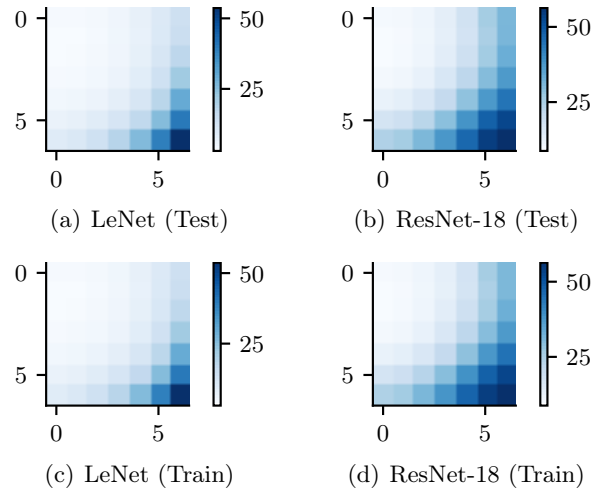


Figure 15: Grid **MNIST** ( $M = 500$ ,  $K = 8$ ,  $T = 3$ )

## I.2 MNIST “flipped”

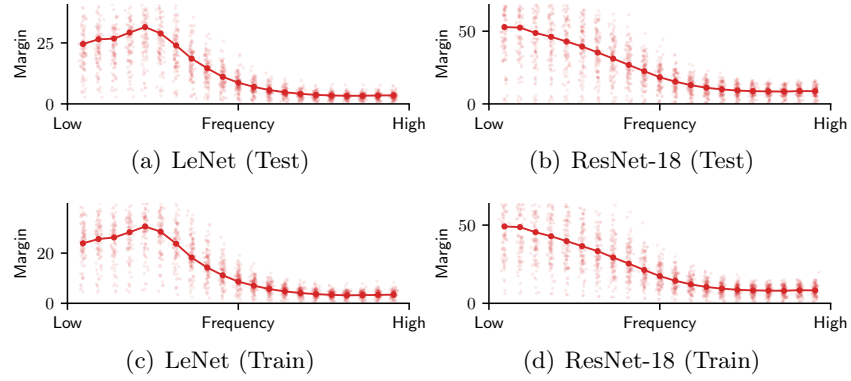


Figure 16: Diagonal MNIST “flipped” ( $M = 1,000$ ,  $K = 8$ ,  $T = 1$ )

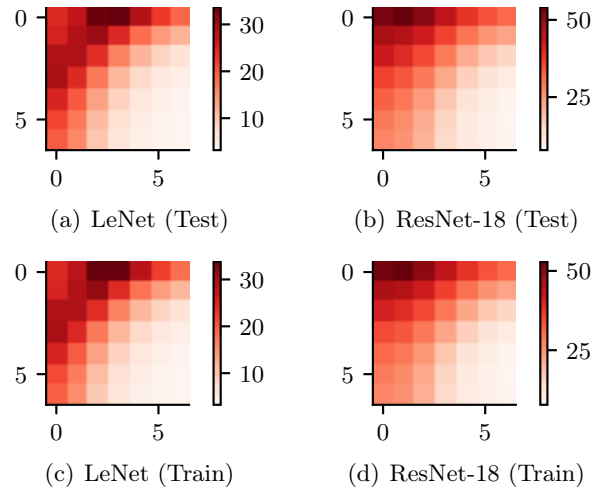


Figure 17: Grid MNIST “flipped” ( $M = 500$ ,  $K = 8$ ,  $T = 3$ )

### I.3 CIFAR-10

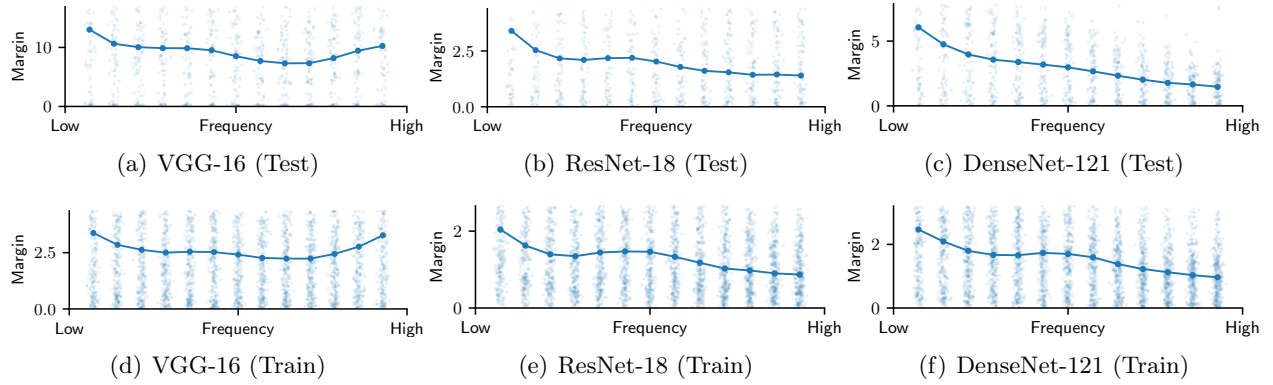


Figure 18: Diagonal **CIFAR-10** ( $M = 1,000, K = 8, T = 2$ )

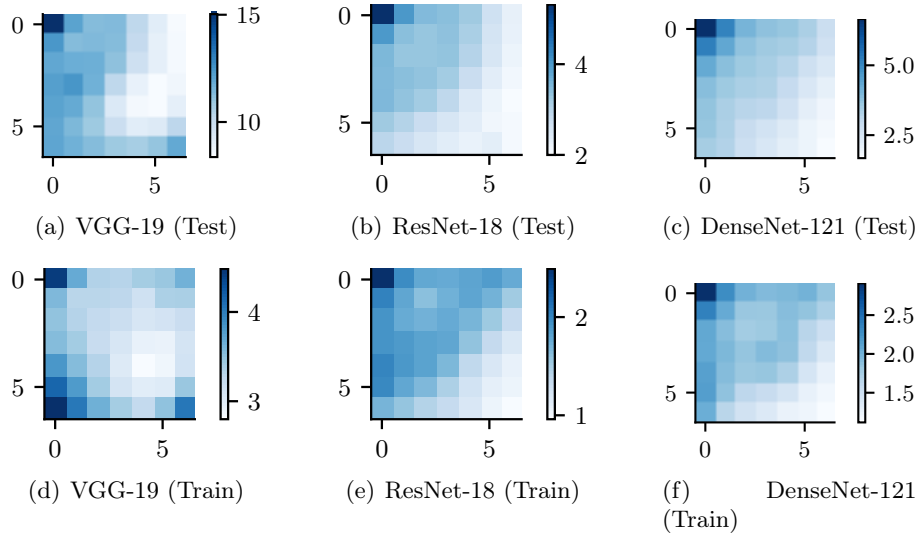


Figure 19: Grid **CIFAR-10** ( $M = 500, K = 8, T = 4$ )

## I.4 CIFAR-10 “flipped”

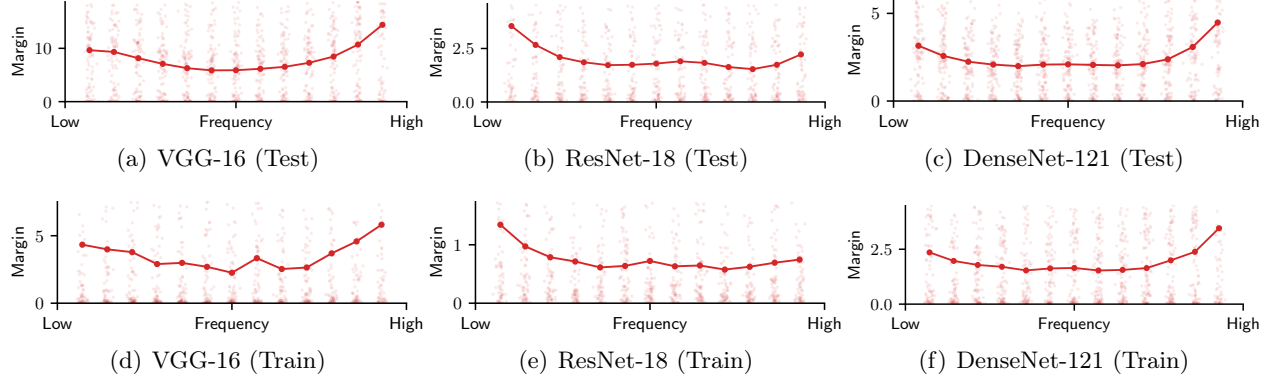


Figure 20: Diagonal **CIFAR-10 “flipped”**

( $M = 1,000$ ,  $K = 8$ ,  $T = 2$ )

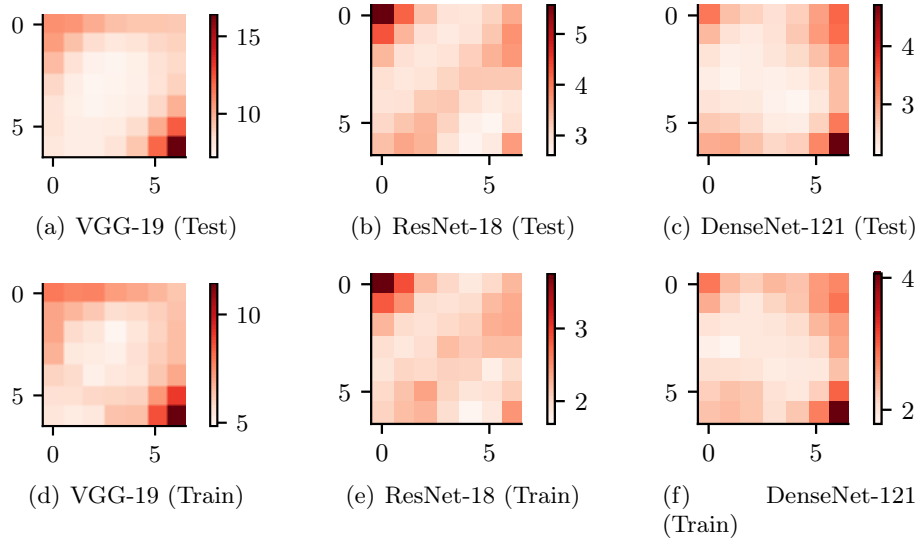


Figure 21: Grid **CIFAR-10 “flipped”** ( $M = 500$ ,  $K = 8$ ,  $T = 4$ )

## I.5 ImageNet

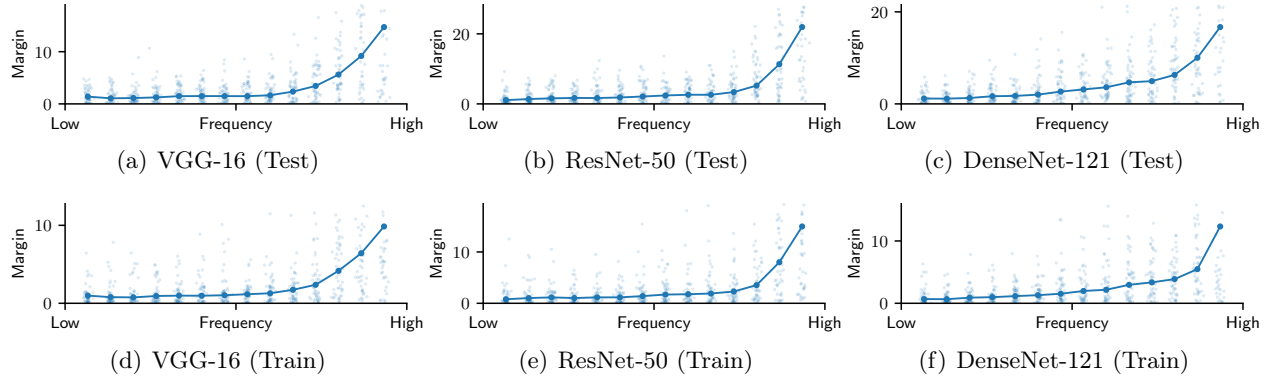


Figure 22: Diagonal **ImageNet** ( $M = 500$ ,  $K = 16$ ,  $T = 16$ )

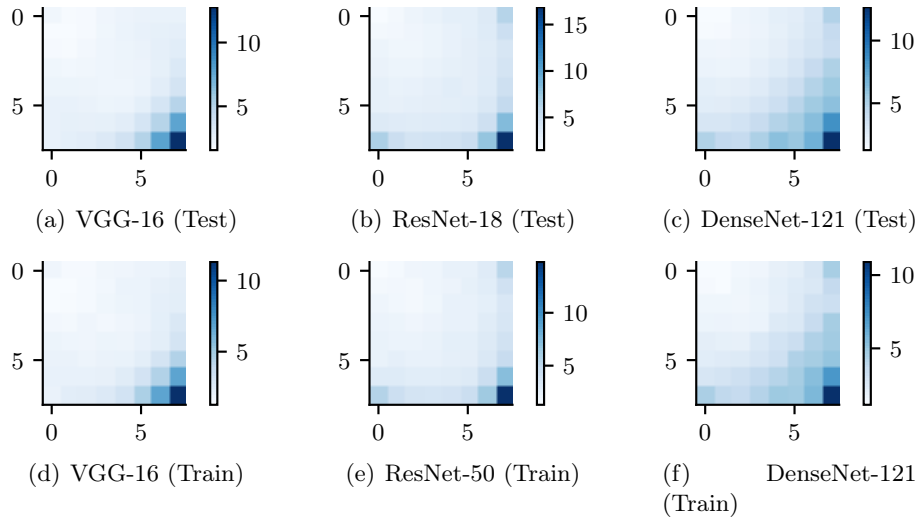


Figure 23: Grid **ImageNet** ( $M = 250$ ,  $K = 16$ ,  $T = 28$ )

## I.6 ImageNet “flipped”

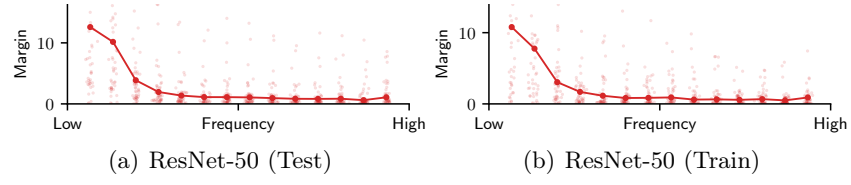


Figure 24: Diagonal **ImageNet** “flipped” ( $M = 500$ ,  $K = 16$ ,  $T = 16$ )

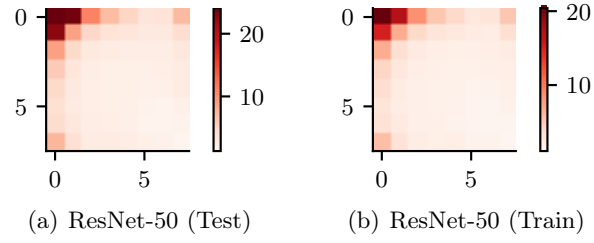


Figure 25: Grid **ImageNet** “flipped” ( $M = 250$ ,  $K = 16$ ,  $T = 28$ )

## J Adversarial training parameters

Table 7 shows the performance and adversarial training parameters of the different networks used in the paper. Note that the hyperparameters of these networks were not optimized in any form during this work. Instead they were selected from a set of best practices from the DAWNBench submissions that have been empirically shown to give a good trade-off in terms of convergence speed and performance. Again, as stated in Section G, especially for the non-standard datasets (e.g., “flipped” datasets), the final performance might not be the best reflection of the highest achievable performance or robustness of a given architecture, since no further hyperparameter tuning was applied.

Table 7: Performance and attack parameters of multiple networks adversarially trained using  $\ell_2$ -PGD. The training parameters are similar to the ones of Table 3. For ImageNet we use the adversarially trained ResNet-50 provided by [37].

DATASET	NETWORK	STANDARD TEST ACC.	ADV. TEST ACC.	EPOCHS	$\ell_2$ BALL RADIUS	STEPS
MNIST	LENET	98.32%	76.01%	25	2	7
	RESNET-18	98.89%	80.26%			
MNIST FLIPPED	LENET	98.29%	74.68%	25	2	7
	RESNET-18	98.75%	81.97%			
CIFAR-10	VGG-19	73.76%	50.15%	50	1	7
	RESNET-18	82.20%	52.38%			
	DENSENET-121	82.90%	54.86%			
CIFAR-10 FLIPPED	VGG-19	71.39%	35.64%	50	1	7
	RESNET-18	73.64%	37.24%			
	DENSENET-121	78.32%	42.32%			
IMAGENET	RESNET-50	57.90%	35.16	—	3	20

## K Description of L2-PGD attack on frequency “flipped” data

Adversarial training [5] is the de-facto method used to improve the robustness of modern deep classifiers. It consists in the approximation of the robust classification problem  $\min_f \max_{\delta \in \mathcal{C}} \mathcal{L}(f(\mathbf{x} + \delta))$  with an alternating algorithm that solves the outer maximization using a variant of stochastic gradient descent, and the inner maximization using some adversarial attack (e.g., PGD). The constraint set  $\mathcal{C} \subseteq \mathbb{R}^D$  encodes the “imperceptibility” of the perturbation.

In our case, when dealing with natural images coming from the standard datasets (i.e., MNIST, CIFAR-10 and ImageNet) we use the standard  $\ell_2$  PGD attack to approximate the inner maximization. This attack consists in the solution of  $\arg \max_{\delta \in \mathcal{C}} \mathcal{L}(f(\mathbf{x} + \delta))$  using projected steepest descent, i.e.,

iterating

$$\delta_{n+1} = \mathcal{P}_{\mathcal{C}} \left( \delta_n + \alpha \frac{\nabla_{\delta} \mathcal{L}(f(\mathbf{x} + \delta_n))}{\|\nabla_{\delta} \mathcal{L}(f(\mathbf{x} + \delta_n))\|_2} \right),$$

where  $\mathcal{C} = \{\delta \in \mathbb{R}^D : \|\delta\|_2^2 \leq \epsilon, \quad \mathbf{0} \preceq \delta \preceq \mathbf{1}\}$ . The projection operator  $\mathcal{P}_{\mathcal{C}} : \mathbb{R}^D \rightarrow \mathbb{R}^D$  can efficiently be implemented as

$$\mathcal{P}_{\mathcal{C}}(\mathbf{x}) = \text{clip}_{[0,1]} \left( \min\{\|\delta\|_2, \epsilon\} \frac{\delta}{\|\delta\|_2} \right),$$

where

$$[\text{clip}_{[0,1]}(\mathbf{x})]_i = \begin{cases} 0 & [\mathbf{x}]_i \leq 0 \\ [\mathbf{x}]_i & [\mathbf{x}]_i < 0 \leq 1 \\ 1 & [\mathbf{x}]_i > 1 \end{cases}.$$

However, when we train using “flipped” data we need to make sure that we also transform the constraint set  $\mathcal{C}$ . Indeed, recall that the goal of training with “flipped” datasets is to check that the margin distribution approximately follows the data representation. Adversarial training tries to maximize the loss of the classifier by finding a worst-case example inside a constrained search space that is parameterized in terms of some properties of the input data (e.g., distance to a sample, or color box constraints). For this reason, if our goal is to check what happens when we only change the data representation but keep the same training scheme, it is important to make sure that adversarial training has the same search space regardless of the data representation. The flipping operator is reversible, which means we can always go back to our initial representation. Hence, by respecting the constraints over the initial representation, we make sure that the resulted adversarial examples in the new representation will still satisfy the constraints when reversed to the initial representation (image space). We achieve this reparameterization efficiently by modifying the projection operator on PGD.

Let  $\hat{\mathbf{x}} = \mathbf{D}_{\text{DCT}}^T \text{flip}(\mathbf{D}_{\text{DCT}} \mathbf{x})$  denote a frequency “flipped” data sample. The  $\ell_2$  PGD attack on this representation solves  $\arg \max_{\hat{\delta} \in \hat{\mathcal{C}}} \mathcal{L}(f(\hat{\mathbf{x}} + \hat{\delta}))$ , where  $\hat{\mathcal{C}} = \{\hat{\delta} \in \mathbb{R}^D : \mathbf{D}_{\text{DCT}}^T \text{flip}(\mathbf{D}_{\text{DCT}} \hat{\delta}) \in \mathcal{C}\}$ . Therefore, the new “flipped” PGD algorithm becomes

$$\hat{\delta}_{n+1} = \mathcal{P}_{\hat{\mathcal{C}}} \left( \hat{\delta}_n + \alpha \frac{\nabla_{\hat{\delta}} \mathcal{L}(f(\hat{\mathbf{x}} + \hat{\delta}_n))}{\|\nabla_{\hat{\delta}} \mathcal{L}(f(\hat{\mathbf{x}} + \hat{\delta}_n))\|_2} \right),$$

where  $\mathcal{P}_{\hat{\mathcal{C}}}$  can be efficiently implemented using Dykstra’s projection algorithm [38]. This is, start with  $\hat{\mathbf{x}}_0 = \hat{\mathbf{x}}, \hat{\mathbf{p}}_0 = \hat{\mathbf{q}}_0 = \mathbf{0}$  and update by

$$\begin{aligned} \hat{\mathbf{y}}_k &= \min \{ \|\hat{\mathbf{x}}_k + \hat{\mathbf{p}}_k\|_2, \epsilon \} \frac{\hat{\mathbf{x}}_k + \hat{\mathbf{p}}_k}{\|\hat{\mathbf{x}}_k + \hat{\mathbf{p}}_k\|_2} \\ \hat{\mathbf{p}}_{k+1} &= \hat{\mathbf{x}}_k + \hat{\mathbf{p}}_k - \hat{\mathbf{y}}_k \\ \mathbf{x}_{k+1} &= \text{clip}_{[0,1]} (\mathbf{D}_{\text{DCT}}^T \text{flip}(\mathbf{D}_{\text{DCT}}(\hat{\mathbf{y}}_k + \hat{\mathbf{q}}_k))) \\ \hat{\mathbf{x}}_{k+1} &= \mathbf{D}_{\text{DCT}}^T \text{flip}(\mathbf{D}_{\text{DCT}} \mathbf{x}_{k+1}) \\ \hat{\mathbf{q}}_{k+1} &= \hat{\mathbf{y}}_k + \hat{\mathbf{q}}_k - \hat{\mathbf{x}}_{k+1}. \end{aligned}$$

The sequence  $(\hat{\mathbf{x}}_k)$  converges to  $\mathcal{P}_{\hat{\mathcal{C}}}(\hat{\mathbf{x}})$ . In our experiments we use 5 iterations of the algorithm as these are enough to achieve a small projection error.

## L Spectral decomposition on frequency “flipped” data

Following the results presented in Section 4.2, we now show in Figure 26 the spectral decomposition of the adversarial perturbations crafted during adversarial training for the frequency “flipped” CIFAR-10 dataset on a DenseNet-121 network. In contrast to the spectral decomposition of the perturbations on CIFAR-10 (left), the energy of the frequency “flipped” CIFAR-10 perturbations (right) remains concentrated in the high part of the spectrum during the whole training process, and has hardly any presence in the low frequencies. In other words, the frequency content of the  $\ell_2$ -PGD adversarial perturbations also “flips” (c.f. Section K and M).

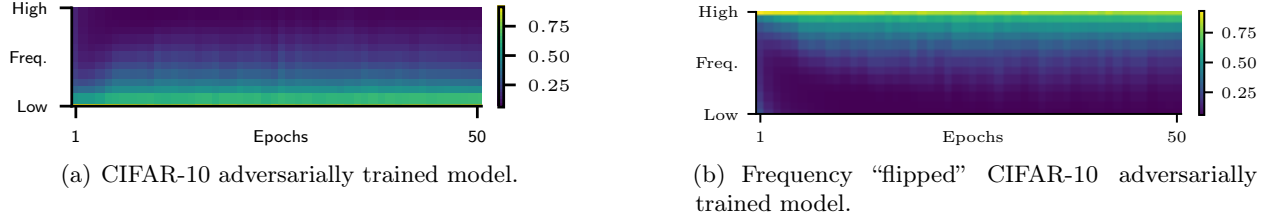


Figure 26: Energy decomposition in subspaces of the DCT diagonal of adversarial perturbations used during adversarial training ( $\ell_2$  PGD with  $\epsilon = 1$ ) on 1,000 (a) CIFAR-10 and (b) frequency “flipped” CIFAR-10 training samples per epoch for a DenseNet-121. The plot shows 95-percentile of energy.

## M Margin distribution for adversarially trained networks

We show here the margin distribution on the diagonal of the DCT for different adversarially trained networks on multiple datasets using the setup specified in Section J. We also show the median margin for the same  $M$  samples on a grid from the DCT.

The first thing to notice for the standard datasets is that, for every network and dataset, there is a huge increase along the high-frequency directions, when compared to the margins observed in Section I. Apart from these, similarly to the observations of Section I, the margins on both train and test samples are very similar, with the differences in the values being quite minimal, while again the trend of the margins with respect to subspaces of different frequencies (increasing from low to high frequencies) is similar in both the grid and the diagonal evaluations. Finally, in every evaluation (diagonal or grid) and for every data set (train or test), “flipping” the representation of the data results in “flipped” margins as well; even for the case of CIFAR-10 where for standard training (Figure 20) the “flipping” was not obvious due to the quite uniform distribution of the margin.

## M.1 MNIST

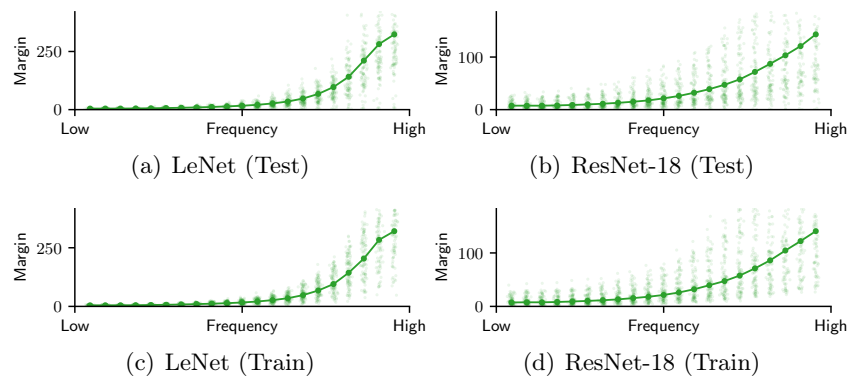


Figure 27: Diagonal **MNIST** adversarially trained ( $M = 1,000$ ,  $K = 8$ ,  $T = 1$ )

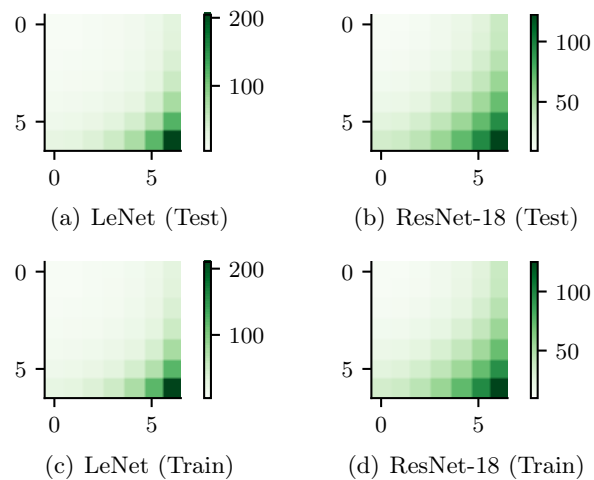


Figure 28: Grid **MNIST** adversarially trained ( $M = 500$ ,  $K = 8$ ,  $T = 3$ )

## M.2 MNIST “flipped”

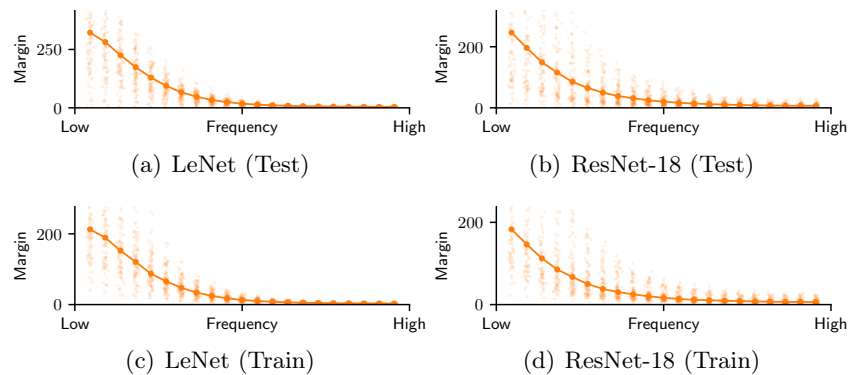


Figure 29: Diagonal MNIST “flipped” adversarially trained ( $M = 1,000$ ,  $K = 8$ ,  $T = 1$ )

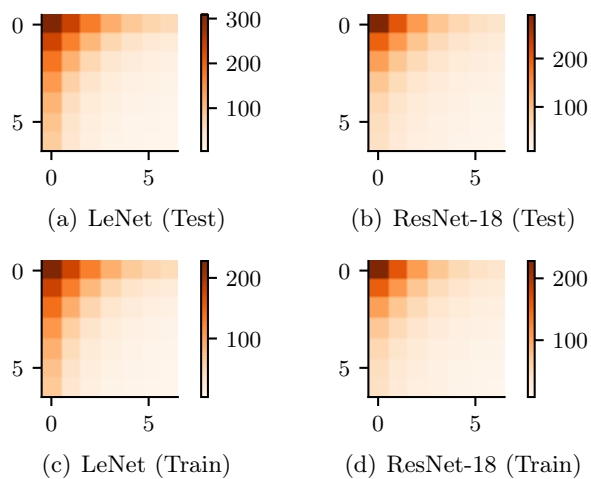


Figure 30: Grid MNIST “flipped” adversarially trained ( $M = 500$ ,  $K = 8$ ,  $T = 3$ )

### M.3 CIFAR-10

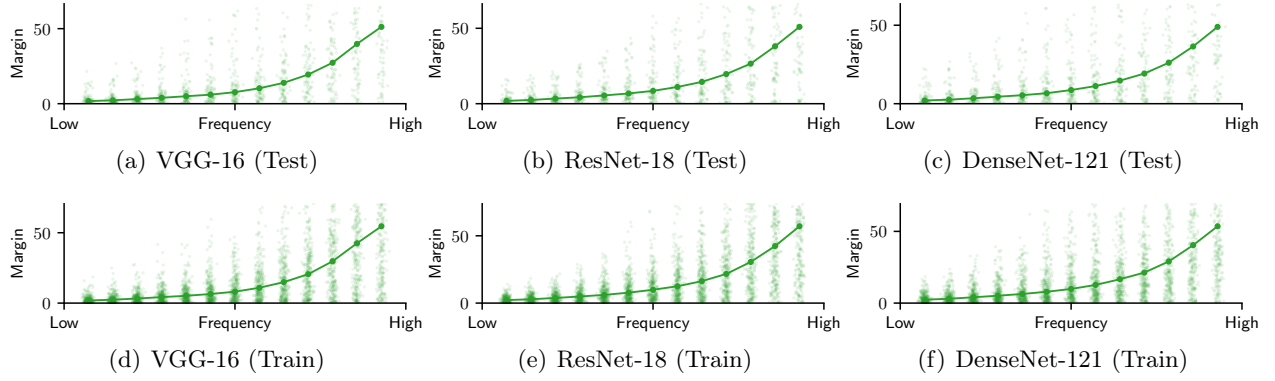


Figure 31: Diagonal **CIFAR-10** adversarially trained ( $M = 1,000$ ,  $K = 8$ ,  $T = 2$ )

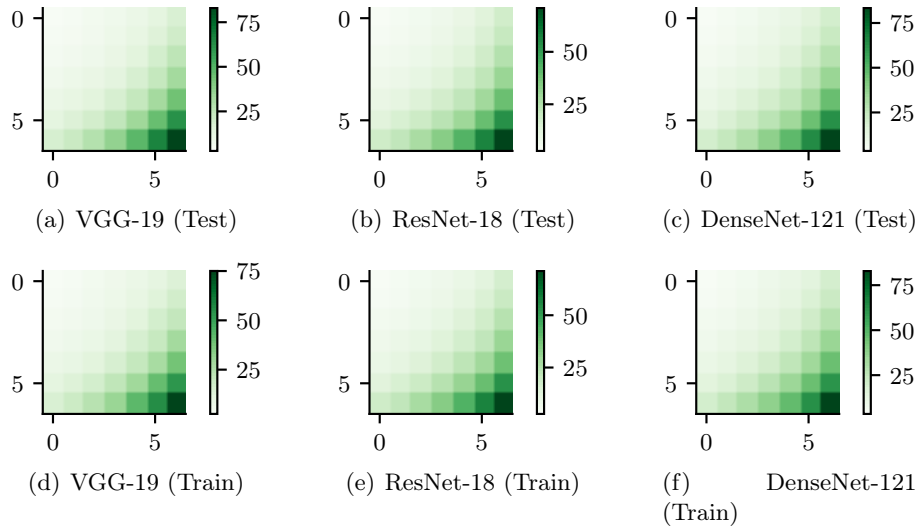


Figure 32: Grid **CIFAR-10** adversarially trained ( $M = 500$ ,  $K = 8$ ,  $T = 4$ )

## M.4 CIFAR-10 “flipped”

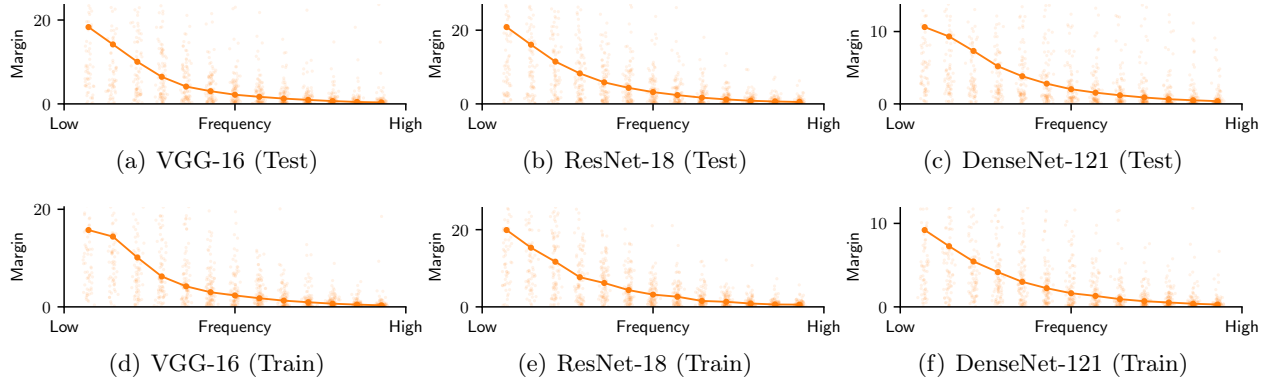


Figure 33: Diagonal **CIFAR-10 “flipped”** adversarially trained ( $M = 1,000$ ,  $K = 8$ ,  $T = 2$ )

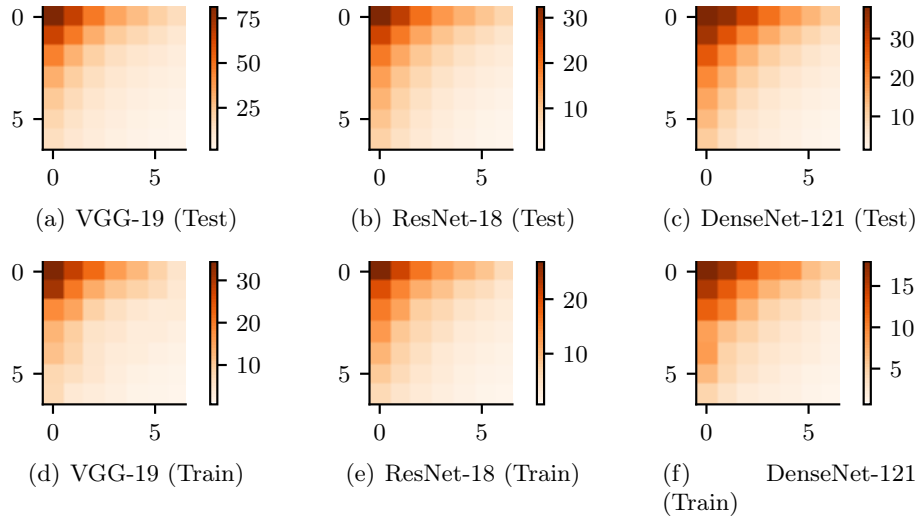


Figure 34: Grid **CIFAR-10 “flipped”** adversarially trained ( $M = 500$ ,  $K = 8$ ,  $T = 4$ )

## M.5 ImageNet

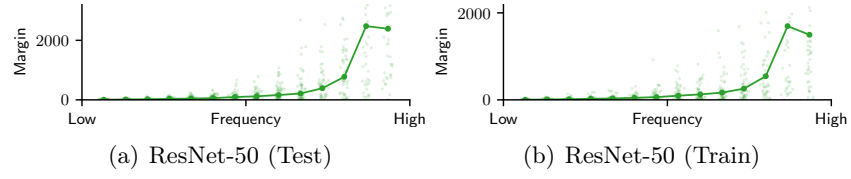


Figure 35: Diagonal **ImageNet** adversarially trained ( $M = 500$ ,  $K = 16$ ,  $T = 16$ )

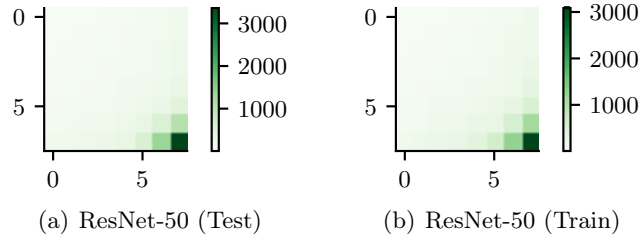


Figure 36: Grid **ImageNet** adversarially trained ( $M = 250$ ,  $K = 16$ ,  $T = 28$ )

## N Margin distribution on random subspaces

Finally we show the same evaluation of Section I performed using a random orthonormal basis instead of the DCT basis to demonstrate that the choice of basis is indeed important to identify the discriminative and non-discriminative directions of a network. Indeed, from Figure 37 it is clear that a random basis is not valid for this task as the margin in any random subspace is of the same order with high probability [39].

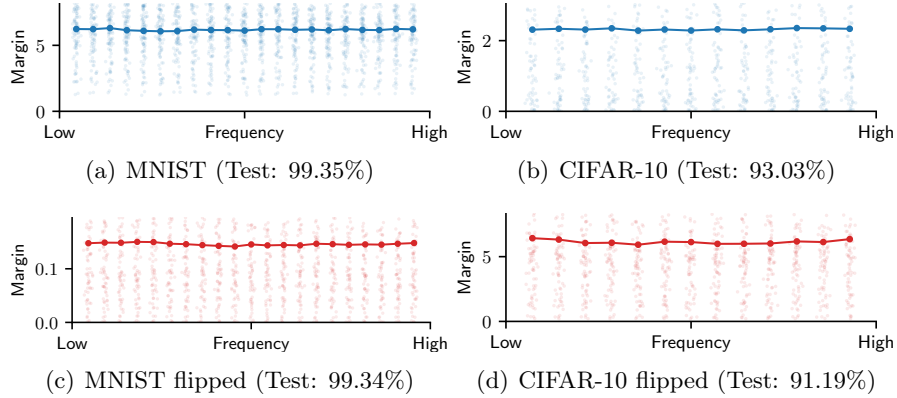


Figure 37: Margin distribution of test samples in subspaces taken from a random orthonormal matrix arranged as a tensor of the same dimensionality as the DCT tensor. Subspaces are taken from the diagonal with the same parameters as before. **Top:** (a) MNIST (LeNet), (b) CIFAR-10 (DenseNet-121) **Bottom:** (d) MNIST (LeNet) and (e) CIFAR-10 (DenseNet-121) trained on frequency “flipped” versions of the standard datasets.